博士論文

Four-dimensional dose calculation using in-treatment cone beam computed tomography and linear accelerator log data

（治療中コーンビーム断層画像と医療用加速器の動作記録を用いた４次元線量分布計算）

早乙女　直也

Abstract

With recent developments, the record and verification system for high-precision radiotherapy during dose delivery plays an important role in quality control and assurance. An investigation of robust techniques for actual dose verification is currently one of the active areas of research in radiation therapy. The aim of this study is to develop a reliable technique of *in vivo* dosimetry for a moving target based on in-treatment data. This thesis is composed of 3 parts; (1) the analysis of log data in the state-of-the-art digital linear accelerator (LINAC) using an electric portal imaging device (EPID); (2) the analysis of the density-override method in dose calculation; and (3) the study of the four-dimensional (4D) dose calculation based on the 2 other studies outlined above.

After the introduction, in Chapter 2, the position of the multi-leaf collimator (MLC) recorded in the log data is analyzed by using the EPID. From the comparison, the difference was 0.88 ± 0.93 mm. As an estimate of the dose difference, an approximately 1-mm difference of MLC position does not effectively affect the dose distribution for the delivery of volumetric modulated arc therapy (VMAT). This result justified the use of the log data for actual dose verification.

In Chapter 3, the influence of the image quality in the dose calculation is discussed. Due to image degradation, it is well known that use of cone-beam computed tomography (CBCT) for dose calculation yields a large uncertainty in dose distribution. In this thesis, the method that utilizes the information of the anatomical mean densities inside the region of interest (ROI) obtained by the treatment planning computed tomography (CT) is employed. Applying the ROI mapping method to the same planning CT as in the original plan for 3 lung cancer patients, the accuracy of the ROI mapping method was within 1.2%.

In Chapter 4, the 4D dose calculation with the ROI mapping method was performed by use of the in-treatment 4D CBCT and LINAC log data, both of which were acquired during treatment. In a study using a moving phantom, 4D dose calculation well reproduced the measurement in comparison with the 3D dose calculation. Actual dose distributions for three lung cancer patients with this technique were compared with those of the plan. A small but significant dose difference between the 3D and 4D calculations was observed for the case of large target traveling. In addition, day-to-day fluctuation of the delivered dose was observed for all the patients.

The importance of *in vivo* dosimetry for a moving target is apparent. The present technique and the findings of this study will contribute to maintain the quality of high-precision radiation therapy.

Abbreviation

GTV: Gross tumor volume

CTV: Clinical tumor volume

ITV: Internal target volume

PTV: Planning target volume

ICRU: International commission on radiation unit and measurement

IMRT: Intensity modulated radiation therapy

VMAT: volumetric arc therapy

SBRT: Stereotactic body radiation therapy

ART: Adaptive radiation therapy

IGRT: Image guided radiation therapy

MLC: Multi-leaf collimator

SMLC: Segmental multi-leaf collimator

DMLC: Dynamic multi-leaf collimator

LINAC: liner accelerator

OAR: Organ at risk

3D: Three-dimensional

4D: Four-dimensional

CT: Computer tomography

CBCT: Cone beam computed tomography

kV: kilo voltage

MV: Mega voltage

RPM: Real-time position management respiratory gating system

EPID: Electrical portal imaging device

QA: Quality assurance

DOG: Difference of Gaussian

TPS: Treatment planning system

ROI: Region of interest

Contents

1 Introduction

1.1 Cancer care

Cancer has been the leading cause of death in Japan since 1981, and its rate has been increasing (Fig. 1-1) [1]. The disease of the most prevalence and relevance for radiotherapy is lung cancer. The lung is the leading site of cancer (23.8% for men, 13.5% for women) (Fig. 1-2). The 5-year survival rate for all stages combined is 36.1% (*Center for Cancer Control and Information Services, National Cancer Center, Japan (Vital Statistics of Japan)*[2].

For cancer, there are 3 types of standard treatment: surgery, chemotherapy, and radiation therapy. Surgery is one of the primary options for isolated solid cancers and may play a role in palliation and prolongation of survival. Cancer is rarely treated by chemotherapy alone. Chemotherapy in addition to surgery and radiation therapy has proven useful in many types of different cancer, including breast cancer, colorectal cancer, pancreatic cancer, testicular cancer, ovarian cancer, and lung cancers, and the others. The effectiveness of chemotherapy is often limited by its toxicity to other normal tissue. Radiation therapy involves the use of ionizing radiation in an attempt to either cure or improve the symptoms of cancer in combination with surgery. Radiation therapy is typically combined with surgery and/or chemotherapy, except for certain types of cancer, such as early head and neck cancer,

in which radiation therapy may be used alone.

The treatments actually used depend on the cancer type, location, and grade of the cancer, as well as the patients' health and wishes. Because of its non-invasive features and recent developments for high-precision treatment, radiation therapy has become an important treatment choice not only for inoperable cases but also for operable cases.

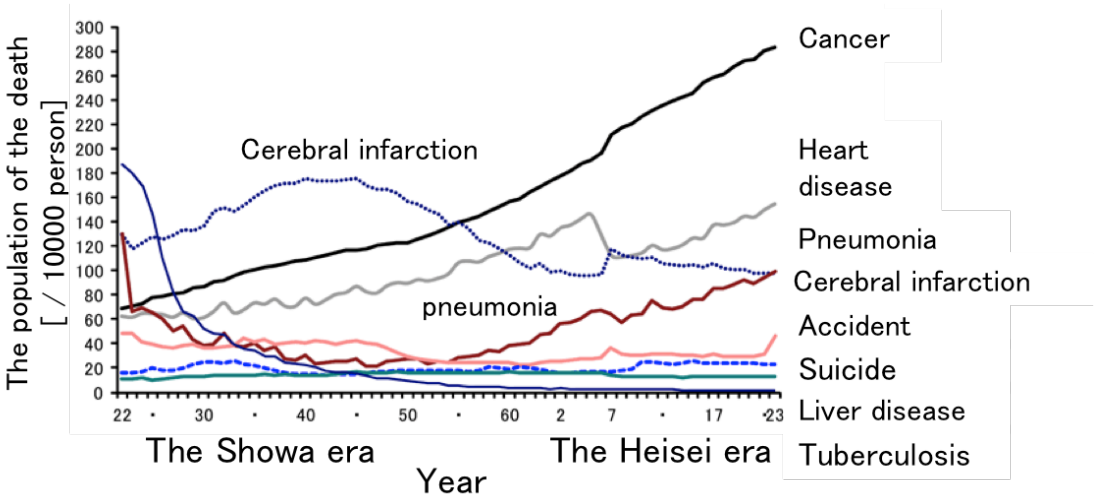

Fig. 1-1: Incidence of deaths in Japan. Cancer has been the leading cause of death in Japan since 1981, and its rate has been increasing. (*Center for Cancer Control and Information Services, National Cancer Center, Japan (Vital Statistics of Japan*)

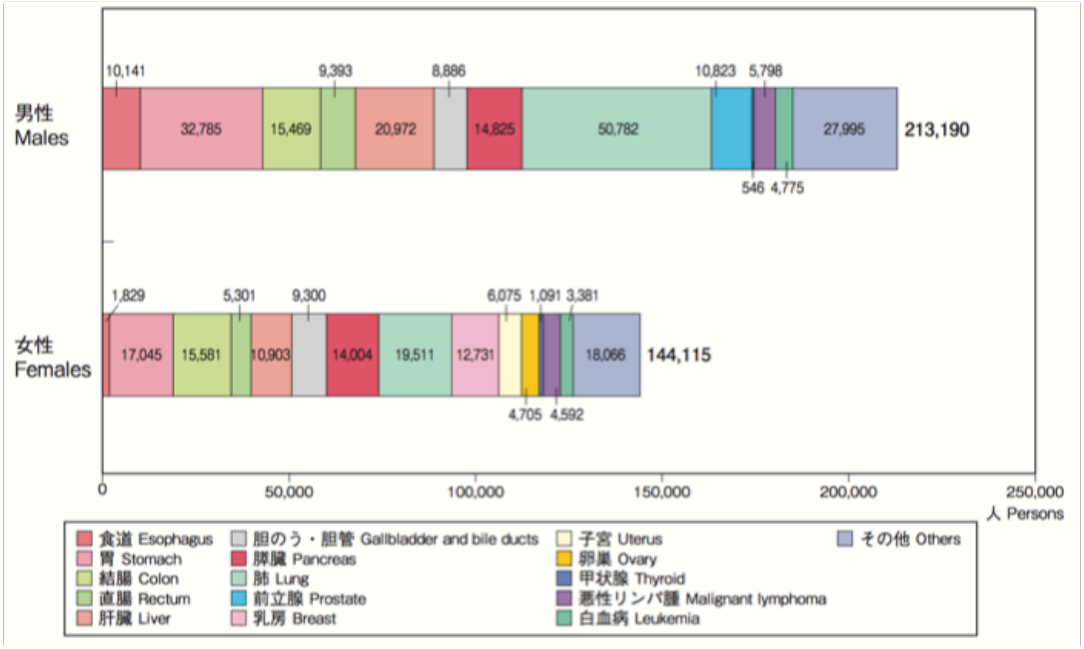

Fig. 1-2: The number of the deaths by cancer site in 2001. The disease of the most prevalence and relevance for radiotherapy is lung cancer. The lung is the leading site of cancer (23.8% for men, 13.5% for women). The 5-year survival rate for all stages combined is 36.1%. (*Center for Cancer Control and Information Services, National Cancer Center, Japan (Vital Statistics of Japan*)

1.2 Radiation therapy

Radiation therapy is commonly applied to the malignant tumor because of its ability to control cell growth. The ionizing radiation works by damaging the DNA of exposed tissue, leading to cellular death. The radiation fields are formed to spare normal tissues (such as skin or organs) close to the tumor, thereby providing a much larger absorbed dose to the tumor than to the surrounding healthy tissue. Besides the tumor itself, the radiation fields may also include the draining lymph nodes if they are clinically or radiologically involved, or if there is thought to be a risk of subclinical malignant spread. The position of the gross tumor by palpation or imaging is called the gross tumor volume (GTV), and the volume increased clinically is known as the clinical target volume (CTV), defined by ICRU 50, 62 and 83 [3-5]. The most important task in radiation therapy is that the prescribed radiation dose is actually delivered to the CTV. To ensure this, it is critical to manage internal target motion during treatment (ex. respiratory movement) and day-to-day setup error (ex. patient position on the table top), including target deformation (ex. change of tumor size due to radiation response) and mechanical uncertainties. Considering these effects, a geometric concept to extend the CTV is defined as the internal target volume (ITV) and the planning target volume (PTV). The ITV is the volume encompassing the CTV and the internal margin, which includes

variations in size, shape, and position of the CTV, whereas the PTV is the volume encompassing the ITV and the setup margin, which includes uncertainties in patient positioning and alignment of the beams during treatment planning and through all treatment sessions.

In principle, local disease control can be improved as the radiation dose is escalated. However, dose escalation is limited because of the side effects. To overcome this limitation, the margin described above should be reduced substantially, and the dose should be locally deposited in the target as much as possible. The margin reducing has to be performed carefully together with verification of dose distribution and of clinical response. It may be happen that the cancer cell will re-grow if actual dose in the target was lacked. In the following section, several types of techniques that permit a margin reduction and a local deposition of the dose will be introduced: intensity-modulated radiation therapy (IMRT) and its rotational version, volumetric modulated arc therapy (VMAT), stereotactic body radiation therapy (SBRT), image guided radiation therapy (IGRT), and adaptive radiation therapy (ART).

1.2.1 High-precision radiation therapy

a) Intensity modulated radiation therapy (IMRT)

A multi-leaf collimator (MLC), originally designed for blocking irradiation fields,

delivers IMRT either by using multiple field segments (called segmental MLC, SMLC, or "step and shoot" IMRT), which can supply a discrete number of intensities [6, 7], or by having the leaves move across the field at a varying rate (called dynamic MLC, DMLC, or "sliding window" IMRT) to deliver the modulated fields [8-11]**.** For both of these techniques, the absorbed dose is distributed by the composite of the complicated MLC configurations. The MLC configuration and the dose intensity to be delivered with its configuration are determined by the optimization procedure with the dose-volume constraint. Details of IMRT optimization will be given in Section 1.2.2. Thus, IMRT provides a higher dose to the target and a lower dose to normal tissues in comparison with conventional treatment. IMRT is a promising technique to improve local disease control and to reduce the risk of side effects.

Donovan *et al*. [12] reported that better absorbed-dose distributions were achieved with IMRT compare to the traditional method. In a follow-up prospective randomized clinical trial, Donovan *et al*. [13] found that the cosmetic effect was significantly worse in patients in the conventional-treatment arm when compared with the IMRT arm. Using a matched case-control methodology for head and neck cancer, Jabbari *et al*. [14] reported that after a decline following radiotherapy, xerostomia and quality-of-life measures improved 6 months after therapy for the IMRT-treated patients but not for the patients treated with conventional radiotherapy.

b) Volumetric modulated arc therapy (VMAT)

IMRT extensively includes a rotational therapy, namely intensity-modulated arc therapy (IMAT). IMAT was first developed in 1995 as a conventional MLC and has the leaf pattern changing continuously as the gantry rotates [15]. To deliver intensity-modulated fields in a gantry angle, several rotational arcs with different MLC patterns are required for IMAT delivery. However, several rotations were not realistic because it was time consuming and the fixed-dose rate delivery prohibited progress of IMAT. Nevertheless, in 2008, a variation of this technique, using gantry rotation and rapid MLC control, was proposed to compensate for the weak points of IMAT [16]. This new delivery technique is called VMAT. VMAT achieved comparable intensity modulation level compared with IMRT [17-19]**.** In addition, VMAT drastically reduced the amount of radiation intensity, known as the monitor unit (MU). Thus, VMAT was found to be able to deliver the desired dose distribution in a shorter time than IMRT. Nowadays, VMAT plays a main role in high-precision radiotherapy treatment.

c) Stereotactic body radiation therapy (SBRT)

Radiosurgery was first described in 1951 by Lars Leksell [20]. The term radiosurgery was selected because of the similarity of this technique to stereotactic neurosurgery. The first target was a brain tumor, which was treated with the Gamma Knife in 1986 [21]. Radiosurgery differs significantly from conventional fractionated radiotherapy.

Namely, by definition, radiosurgery implies a single treatment. The use of a very large number of beams ensures that no individual beam contributes significantly to the cumulative dose, so that the amount of radiation delivered to normal tissues in the beams' paths is minimized. With improvements in linear accelerators (LINAC), image guidance, and immobilization, the principles of radiosurgery are now being applied outside of the brain. SBRT was developed at the Karolinska Institute in Sweden in the 1990s, using a body frame for immobilization [22]. This involves the precise delivery of a high dose of radiation over 5 or less fractions using sophisticated treatment planning to generate steep dose gradients for maximal normal tissue sparing, often aided by various methods of image guidance and motion management. Over the last decade, these techniques have been refined and more widely implemented in the treatment of many cancers, such as early stage non-small cell lung cancer and lung metastases.

Because of the high radiation dose for a fraction (ex. ~12 Gy/fraction in lung cancer), SBRT requires very high confidence in target localization by managing daily setup variability and intra-fraction motion during beam delivery. This fact urged the development of image-guidance methodology in LINAC systems. At this time, SBRT is accompanied with IGRT.

d) Image guided radiation therapy (IGRT)

IMRT, VMAT, and SBRT are able to achieve an ideal dose distribution with high-dose gradients to spare the normal tissue close to the tumor. However, this is not the case when the patient and his/her anatomies change from the situation at treatment planning. The steep dose gradients offered by these high-precision radiotherapies could provide a lower dose in the target and a higher dose in the organ-at-risk (OAR) in the actual delivery than expected from the treatment planning. The uncertainties arising from patient positioning and anatomical changes are considered as the "margin" in the target and the OARs. Of course, the dose delivered with the margin affects surrounding tissues such that to spare these tissues the achievable dose for the tumor is often compromised. IMRT, VMAT, and SBRT combined with IGRT allows for application of tighter margins than conventional radiotherapy.

Three-dimensional (3D) "volumetric" imaging using computed tomography (CT) mounted on the LINAC represents the latest development in the IGRT armamentaria [23]. Cone-beam CT (CBCT) imaging involves multiple kilovolt (kV) radiographs acquired by a large flat-panel detector [24-26]**.** A four-dimensional (4D) CBCT was also extended by sorting kV radiograph images from the patient's respiratory signal before reconstruction [27, 28]. With the 3D or 4D information obtained just prior to treatment, the patient location can be corrected remotely by controlling the treatment couch, and the treatment can be quickly started.

CBCT is a powerful tool for IGRT, but some limitations remain: (1) an uncertainty caused by the intra-fractional motion and (2) a poor image quality in CBCT. In order to evaluate the former effect, CBCT imaging should be performed during treatment. This is called "in-treatment" CBCT imaging. Actually, this is feasible by employing a rotational treatment similar to VMAT [29]. The latter limitation is mainly due to the scatter photons in CBCT geometry, and consequently, the Hounsfield unit (HU) value from CBCT images has a large deviation in comparison with the diagnostic CT images or treatment planning CT. Perhaps more importantly for radiation therapy, because of poor image quality, CBCT images cannot predict the dose distribution with an adequate accuracy. It is worthwhile to investigate an improved method of accurate dose calculation using CBCT because CBCT has the anatomical information captured in the treatment position, which can be considered adaptively in the successive treatment, as described in the next subsection.

e) Adaptive radiation therapy (ART)

CBCT-based IGRT provides accurate registration of the patient location to the treatment planning CT. Thus, the margin required because of setup error can be reduced. However, anatomical deformation and changes in size are not fully addressed by IGRT. Ideally, the complicated anatomical changes, such as tumor shrinkage, are considered adaptively by modifying the original treatment plan, which is constructed based on the

treatment planning CT acquired approximately 1 or 2 weeks before starting the treatment session. This is called ART [30-33].

ART is categorized into 2 approaches: off-line ART and on-line ART. Whereas in off-line ART, a treatment plan is modified based on previous fractions and delivered in the subsequent fraction, in on-line ART, a treatment plan is modified just prior to each treatment fraction. Yan and coworkers extended the idea of off-line corrections to include organ motion [34, 35]. By combining the information of multiple CT scans obtained in the first week of treatment, a better representation can be made of the average position of internal anatomy, and margins can be tailored to individual patients. They indicated that re-planning during the treatment session significantly improved the normal tissue dose and enabled dose escalation for prostate and head and neck cancers. However, for the clinical implementation of ART, there remains a lack of necessary software tools and clinical workflow support.

1.2.2 Physical aspects of high-precision radiation therapy

a) Plan optimization and dose calculation algorithm

One of the prerequisites for the clinical application of IMRT was the development of inverse planning or optimization strategies. This was because it is impossible to give intuitive MLC shapes and the corresponding intensity from the objective dose without any iterative procedure. The standard procedure of IMRT optimization is as follows (Fig. 1-3).

The starting point is to select a set of variable treatment parameters (each leaf location, MU, and so on) whose values have to be adjusted to their optimal setting. Then, the 3D dose distribution is calculated with the initial values. Next, this dose pattern is reduced to the scalar value via the objective function, in which the sum of the quadratic dose deviations from the minimal or maximal dose allowed to the target and the OAR are usually used. The optimization of the treatment plan means minimizing the objective function by treatment parameters. The convergence of this "optimization loop" is broken if a certain threshold value for the relative change in objective function between 2 subsequent iterations is exceeded.

Dynamic arc optimization (namely VMAT) is achieved by adding several steps. After basic parameters such as an arc range have been forwardly determined, coarse segments are generated in the optimization step, and the MLC segments are created and distributed in 2 different angles (Fig. 1-4). The MLC segments are filtered, evenly redistributed around the arc, and interpolated segments are added to reach the final fine arc spacing.

Optimization for VMAT is likely to produce mechanically unacceptable leaf travel and rotation speed. To avoid this, the machine constraints for maximum leaf travel per gantry angle, the maximum leaf speed, the minimum and maximum dose delivery per gantry angle, and the maximum gantry speed are included in the optimization. The machine constraints can be varied for the treatment sites, i.e., the slow MLC speed is constrained on the optimization

for the moving target, such as in lung cancer.

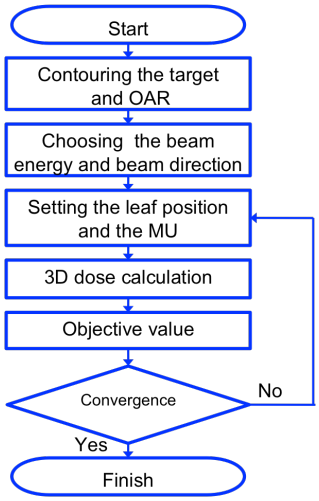

Fig. 1-3: A typical calculation process in IMRT (see text).

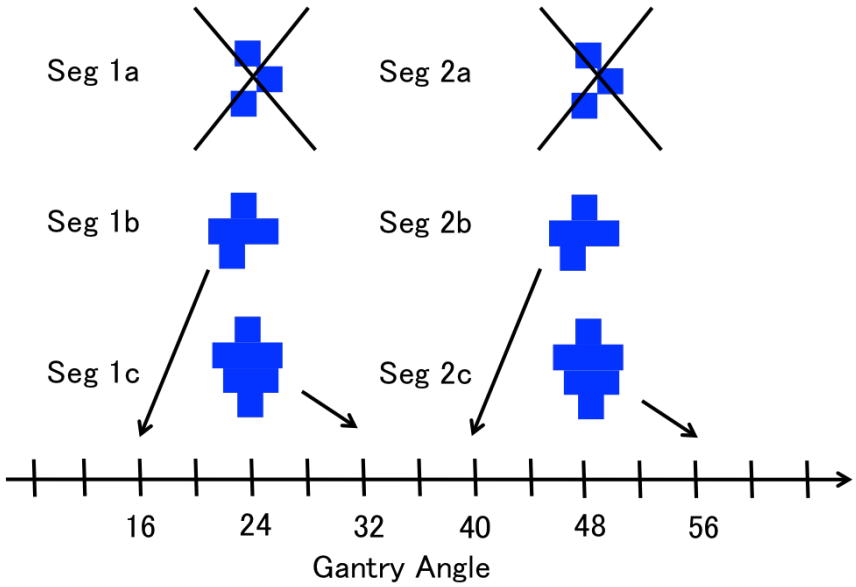

Fig. 1-4: Multileaf collimator (MLC) determination process in VMAT. After basic parameters such as an arc range have been forwardly determined, coarse segments are generated in the optimization step, and the MLC segments are created and distributed in 2 different angles [36].

b) Quality assurance (QA)

A quality assurance (QA) procedure for IMRT has been demanded to ensure that the patient receives the prescribed dose as accurately as possible. In general, the patient specific QA is performed by using phantoms and dosimeters at least 1 day before treatment. However, advances in radiation therapy have increased the accuracy requirements for dose delivery to patients during treatment, ensuring a high level of accuracy for treatments designed to achieve adequate tumor control and reduction of normal tissue complications. One of the IMRT QA criteria during treatment is to verify the treatment parameters, such as MLC motions, with that recorded on the log data. The limitation belongs to the fact that the recorded data in the log data should be verified itself, since the LINAC is controlled by them. For example, the displacement of the beam axis due to gantry rotation cannot be involved. *In vivo* dose measurements using diode, TLD, and MOSFET dosimeters have also been used. The limitation of *in vivo* dosimetry is that the absorbed dose at only 1 or a few points is determined [37]. It is possible to use a multi-element detector to determine the actual absorbed dose delivered to the patient [38]. McNutt *et al*. (1996) first demonstrated the reconstruction of the absorbed dose delivered based on a CT scan of the patient obtained at the time of treatment and using a portal-imaging system to measure the absorbed dose. Since then this has been an active area of investigation.

There are 2 day-to-day variations that must be considered in absorbed dose reconstruction: the variation of the patient anatomy or setup, and the variation of the incident intensity pattern. Of these 2 variations, the patient-related one is more critical because a setup error, weight gain or loss, and tumor shrinkage or growth can greatly perturb the planned absorbed dose distribution [39].

1.3 Radiation therapy for moving target

1.3.1 Organ motion

Motion management becomes very important in the era of high-precision radiation therapy. Organ movement may be divided into 2 general categories: inter-fraction and intra-fraction. The former affects day-to-day target position changes, which is the cause of error in patient setup. This affect can mostly be compensated for by precise target localization before delivering each radiation fraction with image guidance, as described in 1.2.1(d). On the other hand, the latter category, which is caused by respiratory, musculoskeletal, cardiac, and gastrointestinal systems, cannot be taken into account even if IGRT was implemented. Of these 4 systems, much research and development to date has been directed towards accounting for respiratory motion. Previous study of the respiratory motion leads to the following conclusion: there are no general patterns of respiratory behavior that can be assumed for a particular patient prior to observation and treatment. The many individual

characteristics of breathing—quiet versus deep, chest versus abdominal, healthy versus compromised, etc.—and the many motion variations associated with tumor location and pathology lead to distinct individual patterns in displacement, direction, and phase of tumor motion [40-45].

Therefore, the actual information on motion and deformation must be acquired for individual patients. Currently, in most cases, this is done by taking measurements of fiducial positions. In order to address deformation during motion-compensated treatment, fast 4D imaging would be required. In this context, 4D CT acquired single-slice, multi-slice, or cone-beam acquisition can be used; one can obtain 3D data on tumor position at several points along the breathing cycle. Further, 4D cone-beam CT immediately before treatment [28] and during treatment [46] has been recently developed.

In recent years, there has been an increased interest in interventional strategies for managing such motions in radiation treatment. These can be divided into 3 categories: a) ignoring respiration during treatment, b) freezing the motion, and c) tumor tracking.

1.3.2 Radiation therapy for lung tumors

a) Ignoring respiration during treatment

In case of limited tumor mobility, it may be sufficient not to take any measures to control respiratory motion during treatment, provided that it is properly accounted for during

imaging for treatment planning. Respiration is an important source of error in a planning CT scanning of the thorax or abdomen, resulting in respiratory induced motion artifacts that adversely affect the accuracy of target and non-target organ definition. Motion artifacts give rise to a systematic error in tumor position and extent, i.e., the tumor observed in the image is not the respiration-average position [47-49]. CT acquisition techniques that include the range of tumor motion with respiration are available. Using such techniques, one can obtain an image that is representative of the respiration-averaged position of the tumor at the time of simulation. Under the assumption that systematic error is thereby removed, van Herk has concluded that the margin for respiration during treatment is only 30% of the peak-to-peak tumor excursion [50]. For the majority of lung tumors with peak-to-peak amplitudes of 1cm or less, the margin for respiration is a few millimeters, which is added in quadrature with other error sources. It is important that the average tumor position at treatment period may differ from that at simulation; thus, the assumption of no systematic error may break down [51]. This fact implies that some amount of systematic tumor displacement may be present during treatment despite attempts to remove it at simulation, and that image-based monitoring is required to ensure that systematic error does not exceed the assumed value [52, 53].

b) Freezing the motion

Two different strategies have evolved to "freeze" respiratory motion during

radiation treatments: respiratory gating of the accelerator while the patient breathes normally, and controlled patient breathing. In respiratory-gated treatment, delivery of radiation occurs only during certain time intervals, synchronous with the patients' respiration. Respiratory-gated radiation therapy has been in clinical use for over a decade in Japan [54, 55]. Hokkaido University has developed a gated linear accelerator system using real-time fluoroscopic tracking of gold markers implanted in the tumor [56, 57]. In the U.S., the University of California at Davis has reported on a gated radiotherapy system, developed jointly with Varian Medical Systems, which accepts respiratory signals from a video camera (now commercially available as the Real-Time Position Management Respiratory Gating System, or RPM) [58].

In contrast to respiratory-gated radiotherapy, breath control methods exploit anatomical immobilization to minimize the effects of respiratory motion. For example, there is a technique that employs a stereotactic body frame with a flexible compressing plate against the abdomen, which minimizes tumor excursion while still permitting limited normal respiration [59]. For utilizing a predefined lung volume, there are 2 approaches that have been in clinical use: active breathing control [60] and voluntary deep inspiration breath-hold [61-63]. In the former approach, the device suspends patient breathing at any pre-determined position in the normal respiratory cycle or at active inspiration. It consists of a digital

spirometer to measure respiratory volume, which is in turn connected to a computer-controlled balloon valve. The latter approach involves verbally coaching the patient to a reproducible deep inspiration breath-hold during simulation and treatment. The patient, with a nose clip, breathes through a mouth-piece connected via flexible tubing to a spirometer.

c) Tumor tracking

The third category for managing respiratory motion during treatment is tumor tracking, which consists of 2 major aspects: real-time localization of and real-time beam adaptation to a periodically moving tumor. Tumor-tracking techniques potentially offer additional benefits such as higher delivery efficiency and less residual target motion compared to the "freezing" methods. These factors may be some time important, such as in radiosurgery to thoracic and abdominal tumor sites, where a large dose is delivered during a single relatively lengthy treatment. Delivering a large dose at 1 time requires high dose conformity to the target, and the lengthy treatment time demands a high degree of dose delivery efficiency. It is important that real-time beam adaptation is not feasible without precise real-time localization of the tumor position `in 3 dimensions. Owing to system latency and the desire to reduce the imaging dose, predictive filters are usually required for anticipating tumor position in a short period of time after localizing it at 1 time point. Errors

in localization should be identified in real-time in order to avoid irradiating the wrong target. Various aspects of tumor tracking have been developed (see references [64-69]).

1.3.3 Problems

IMRT has seen widespread application because of its ability to generate more effectively to the spatial distribution of the dose deposited in a patient. The implications for targets in the thoracic and abdominal regions have been particularly important because of the many OARs in these regions. However, organ motion presents as a considerable issue for IMRT delivery, since beam-intensity gradients are no longer confined solely to the edges of the beams. Rather, such gradients can be inside the field defined by the primary collimators. Thus, if a target is also moving inside this same field with its own period unique from the MLC leaves and possibly deforming, it is easy to understand why there are concerns over the use of IMRT with targets affected by motion [70-74].

It was seem that the concern over potential dosimetric error introduced by respiratory motion for IMRT treatments is justified; Yu *et al*. [75] showed that fluence variations within a moving target tend to average out over the typical course of 30 or more fractions when one assumes that the breathing phase or frequency is random from day to day. Along similar lines, Bortfeld *et al*. showed that dosimetric errors introduced by respiratory motion also tend to average out with fractionation [76-80]. However, these studies assumed or

applied simplistic, 1-dimensional motion, which can be quite different from the real, complex respiratory phenomenon [81, 82]. Furthermore, target deformation may be present, although this deformation has yet to be quantified. Therefore, they cautioned that fractionation alone should not be relied upon, at least in cases of > 1 cm motion, until their findings could be verified under more realistic conditions.

The above studies indicate that caution is warranted when considering IMRT for targets subject to respiratory motion, particularly for single or few-fraction treatments common for SBRT. For individuals who still intend on using IMRT without any direct motion correction strategy, it needs to be emphasized that the full extent of breathing motion should be assessed and considered when assessing margins for the treatment plan. Even with correction strategies, there can still be residual target motion with respect to the beam, such as with respiratory-gated treatment, which may exhibit similar, albeit smaller, effects (also the potential problem of the respiratory-gated treatment is its ineffectiveness to deliver the beam).

The verification of IMRT for a moving target involves reconstructing the dose profile actually delivered to the individual patients from "the data" acquired during treatment. The beam information at which the tumor location is identified from the respiratory signal can be obtained by the log data or electronic portal-imaging device (EPID). The simplest way to acquire the respiratory information is to utilize an external respiratory monitoring system,

such as an RPM. However, internal-external correlation could be disturbed by transient changes in breathing [82]. Naturally, the best correlation is obtained by monitoring the direct trajectory of the tumor with kV radiographs. By accompanying the rotational treatment, kV imaging during treatment adds to produce in-treatment 3D information, with which the dose calculation can be performed.

1.4 Purpose of this thesis

Since 1980's the conformal arc irradiation for small lung tumor has been applied in the University of Tokyo Hospital. In 1990's, in-room CT and megavoltage (MV) CT were developed for the verification of the target position [83]. Recently, the in-room 3D and 4D CBCT systems were also developed [84]. Thus, patient's tumor motion during treatment can be acquired with volume information.

In this thesis, I aim to establish dose verification for high-precision lung SBRT using VMAT. The absorbed-dose distribution in every fraction of 1 treatment course was reconstructed on in-treatment 4D CBCT and with the recorded log data for LINAC machine parameters. The in-treatment 4D CBCT currently includes the most reliable data for tumor position during treatment. The respiratory signals used in the in-treatment 4D CBCT reconstruction were synchronized with the beam information in the log data. Thus, the complete observation-based dose distribution was reconstructed for each respiratory phase of

each fraction.

The criticisms for the use of LINAC log data in the QA, described in 1.2.2(b), are discussed in Chapter 2 by comparing it with MLC detection using an EPID. It is still a problem to employ CBCT in the dose calculation. The HU in CBCT has a location dependency in the reconstruction space. One of the main sources of this dependency is caused by scattering from the scanned object. Therefore, in this thesis, the anatomical mean densities inside the region of interest (ROI) obtained by the treatment planning CT were overridden by those identified on the CBCT. Hereafter, this is called the ROI mapping method. The accuracy of the dose calculation using the ROI mapping method is assessed in Chapter 3 by comparing calculations with and without override in treatment planning CT. In Chapter 4, 4D dose calculations for a moving phantom and 3 lung cancer patients are performed. The doses for center-of-mass location, and mean dose of the tumor are compared with those expected from the treatment planning. In Chapter 5, the present result is compared with the previous studies and the importance of dose verification is indicated. Finally, the summary and future remarks are given in Chapter 6.

1.5 Ethical considerations

Irradiating of the kV X-ray in the verification purpose for the organ motion at the same time as in the irradiating of the MV X-ray for the treatment has been permitted by a

notification No. 0417009 of the Ministry of Health, Labour and Welfare dated 17th April 2007. The use of the radiotherapy database for comprehensive and retrospective research has been approved by the committee of the Ethical Review Board in the University of Tokyo Hospital (No. 3372). This research was performed with prior written informed consent. The data was transferred into anonymous one. It makes a definite promise not to use any purpose except this research and to rigid information control.

2 Verification of the log data by MLC detection using an EPID

2.1 Introduction to Chapter 2

From the viewpoint of quality assurance in radiotherapy, it is important to understand what the LINAC is doing during irradiation. The impact of the systematic geometrical error has been shown by many researchers [86-88]. The effect of the random mechanical error for VMAT has also been investigated [89-92].

Dose reconstruction using log data assumes that the recorded log data rigorously reproduces the actual beam delivery [93, 94]. In principle, however, the log data can be different from the actual state, and in this case, it is impossible to detect such an error arising from the log data approach. Therefore, it is very important to verify the reliability of the log data using another independent QA system.

An EPID is one of the tools used to observe real-time radiation information from the X-ray transmission. In particular, the field shape analyzed from an EPID may provide an independent verification of the MLC location recorded in the log data. In this chapter, the performance of MLC detection using an EPID is compared with that using the log data, and the error in the dose caused by the uncertainty of MLC position in log data is described.

2.2 EPID imaging, MLC detection algorithms, and log data

2.2.1 EPID properties

An EPID mounted on the opposite site of the gantry head of an Elekta Synergy accelerator at the University of Tokyo Hospital was shown in Fig. 2-1. The EPID is often used for the verification of the patient setup, monitoring of the patient position, regular quality assurance of the MLC position, and so on. During beam delivery, EPID images were sequentially collected with an interval of 0.46 sec using Elekta iViewGT software. The EPID image consisted of 1024 × 1024 pixels with a size of 0.25 mm at the isocenter. Due to limitations of the Elekta iViewGT software, the maximum number of portal imaging sequential acquisitions was only 256. In addition, the iViewGT did not have gantry information. In order to connect the EPID images with the corresponding gantry angles, a gantry angle sensor (Math Resolutions Co.) was independently employed.

To detect the MLC position using EPID, the geometrical invariance of the EPID position has to be checked in advance. The reproducibility of the EPID panel position was measured by the in-out test at various gantry angles (measurement just after closing and opening the EPID panel) and the rotational trajectory. In this measurement, an 8-mm diameter ball bearing (BB) phantom designed for the Wiston-Lutz test was used, and the canter of the BB on the EPID image was captured.

Fig. 2-1: An electronic portal imaging device (EPID) mounted on the linear accelerator (LINAC) (Elekta). The detector panel is a PerkinElmer Amorphous Silicon (a-Si) detector, and provides a resolution of 1024 × 1024 16-bit pixel images, with a detector panel size of 41 × 41 cm (approximately 26 × 26 cm at isocenter). Image data is read from the panel, through a data link into a framegrabber in the iViewGT™ (Elekta).

As a result, the standard deviation of the reproducibility in the in-out test was less than 0.2 mm. The geometric non-idealities were also measured for a rotational irradiation with 3 cm × 3 cm fields. Figure 2-2 shows an example of the non-idealities as a function of the gantry angle (it is called the “flexmap”). With the flexmap, correction was performed for each portal image. The reproducibility of the trajectory with the gantry rotating over 3 months was less than 0.4 mm at the same gantry angle (Fig. 2-3). The reproducibility was evaluated by the difference between each flexmap and the average flexmap over the 3 months at the same gantry angle.

The signal response from the beam intensity in EPID also influences the performance of MLC detection. To see the behavior of the response in EPID, the output

linearity was measured with various beam intensities before using it for MLC detection. The result is shown in Fig. 2-4. The outputs were proportional to the irradiated dose for all energies. Therefore, no intensity correction was performed through the MLC detection using EPID.

With these properties, it is expected that MLC position can be detected within 0.4 mm reproducibility in EPID imaging.

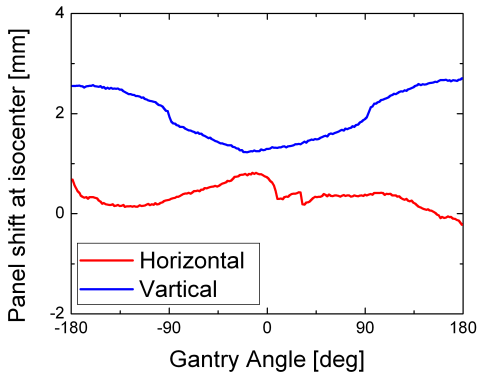

Fig. 2-2: Example of flexmap correction. The radiation center of the flat panel detector can be shifted during gantry rotation for the mechanical reason. This shift is corrected by the flexmap. The red and blue curves indicate the correction for the vertical and horizontal directions in EPID panel, respectively.

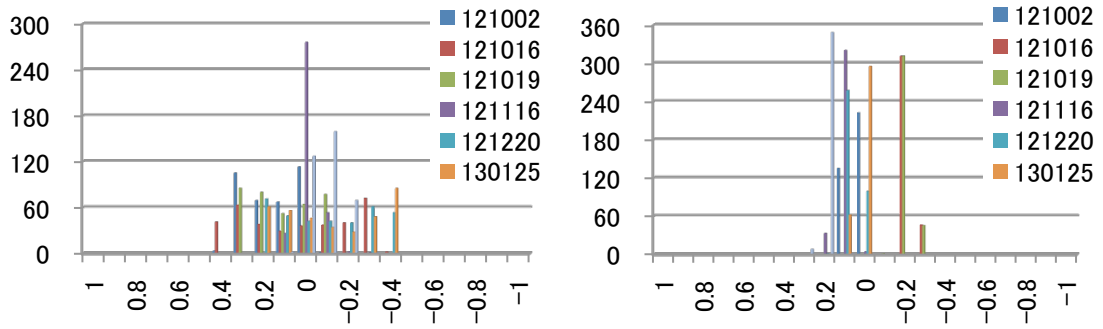

Fig. 2-3: Histogram of the difference of the flexmap over 3 months. Each difference was determined by the distance between each flexmap and the average flexmap over 3 months.

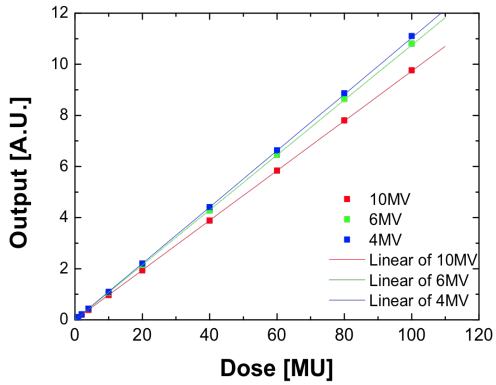

Fig. 2-4: Signal response in EPID. The output is linear as a function of the beam intensity. MU, monitor unit.

2.2.2 MLC detection algorithm

An in-house program to detect the MLC position from the EPID was developed. Although there are a number of gradient-based edge detection techniques available [95, 96], in this study, I employed a difference of Gaussian (DOG) algorithm. This is indicated in the right panel of Fig. 2-5, in which 2 lines where Gaussians are convolved for MLC moving direction with an EPID image after 3 × 3 median filtering are generated. For Gaussian convolutions, a normalized Gaussian distribution (equation below) was employed,

$$G(x) = \frac{1}{\sqrt{2\pi}\sigma}\exp\left[-\frac{x^2}{2\sigma^2}\right] \tag{2-1}$$

$$F(x) = f(x) \otimes G(x) \tag{2-2}$$

Here, $G(x)$ is the Gaussian function, $f(x)$ is the original signal, and $F(x)$ is the Gaussian convolved signal. The square roots of variance (σ) with 0.75 mm ("small Gaussian") and 6.25 mm ("large Gaussian") are used. The symbol $\otimes$ indicates the convolution operation. The MLC position is then determined by zero-crossing position in the difference image between "small Gaussian" and "large Gaussian" images. Typically, the MLC position is detected by use of the threshold value. The difference of the performance between the threshold and DOG methods was investigated by employing various test fields shown in the next subsection.

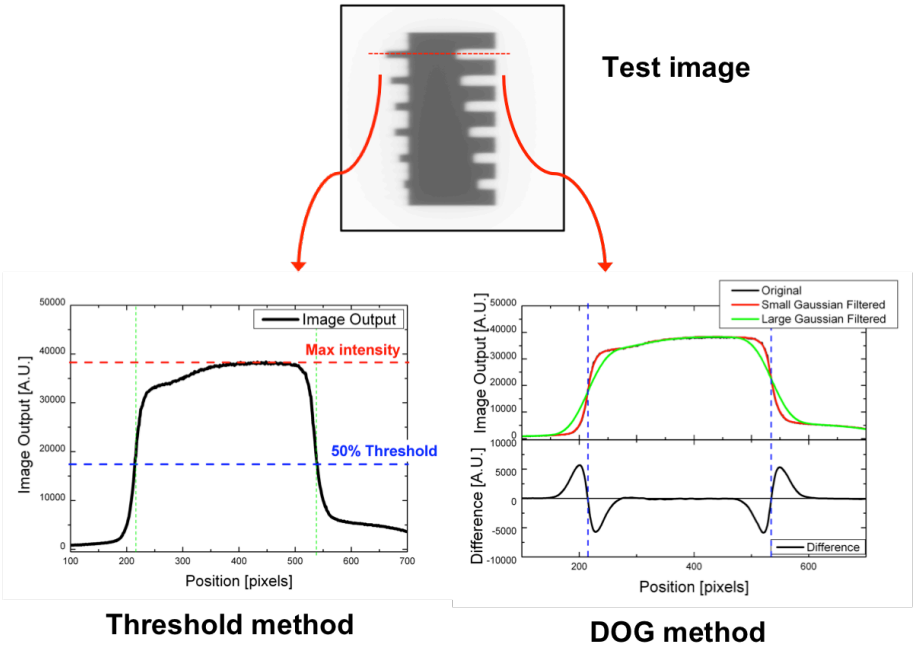

Fig. 2-5: Multileaf collimator (MLC) detection from the electronic portal imaging device (EPID) used in this study; threshold (left panel) and difference of Gaussian (DOG) (right panel) methods (see text).

2.2.3 The Performance test in EPID imaging

Typically, the MLC position is detected using the threshold value. In this subsection, the DOG algorithm is compared with the threshold, as indicated in Fig. 2-5, where the maximum signal is first detected in the line of a specified MLC after 3 × 3 median filtering, and the threshold positions set by 45%, 50%, 55%, and 60% of this maximum value are identified. Thus, the MLC position in each threshold value is regarded as the corresponding threshold position.

The portal images in EPID used in the performance test are listed in Fig. 2-6, where 20 MUs are delivered in each image and the gantry angle is set at 0 degrees. Here, the offsets of the field were set at 0, ± 5, and ± 10 cm, and the positions of the 3 leaves generating the convex or concave shape were set at 1, 2, 3, and 6 cm from the other leave's position, with the distance between the left and right leaves set as 10 cm. No phantom was placed. All the test images were obtained by static irradiation.

The positions of 10 MLC pairs were analyzed. The average error and 1 standard deviation are indicated in Table 2-1 and Fig. 2-7. The DOG method was best in the standard deviation. Figure 2-8 indicates the comparison of the shift level dependence for the threshold method with 55% level and DOG method. The shift level means the distance of 1 convex or concave leaf from the other leaves. The DOG algorithm would be more robust than the

threshold algorithm because the convolution of the Gaussian function with an appropriate width removed the noise in the EPID image. This is advantageous in the clinical application; X-ray attenuation in patients affects the MLC detection in the threshold method, whereas this affect is suppressed by the DOG method.

Unlike above performance test, the field is changed continuously during VMAT delivery. It is estimated that the MLC may move 0.07 cm in an image acquisition with 0.46 sec period. The maximum leaf speed is limited to 0.1 cm per gantry angle for a lung VMAT plan in our hospital. This is almost 0.15 cm per sec for 240 sec irradiation. Therefore, a maximum 0.07 cm blurring could occur during clinical EPID image acquisition; consequently, it may happen that less than 0.04 cm is missing from the MLC detection.

In this test, the DOG method gave a better result than the threshold value method. This is the reason why the DOG method is employed in the verification of the log data.

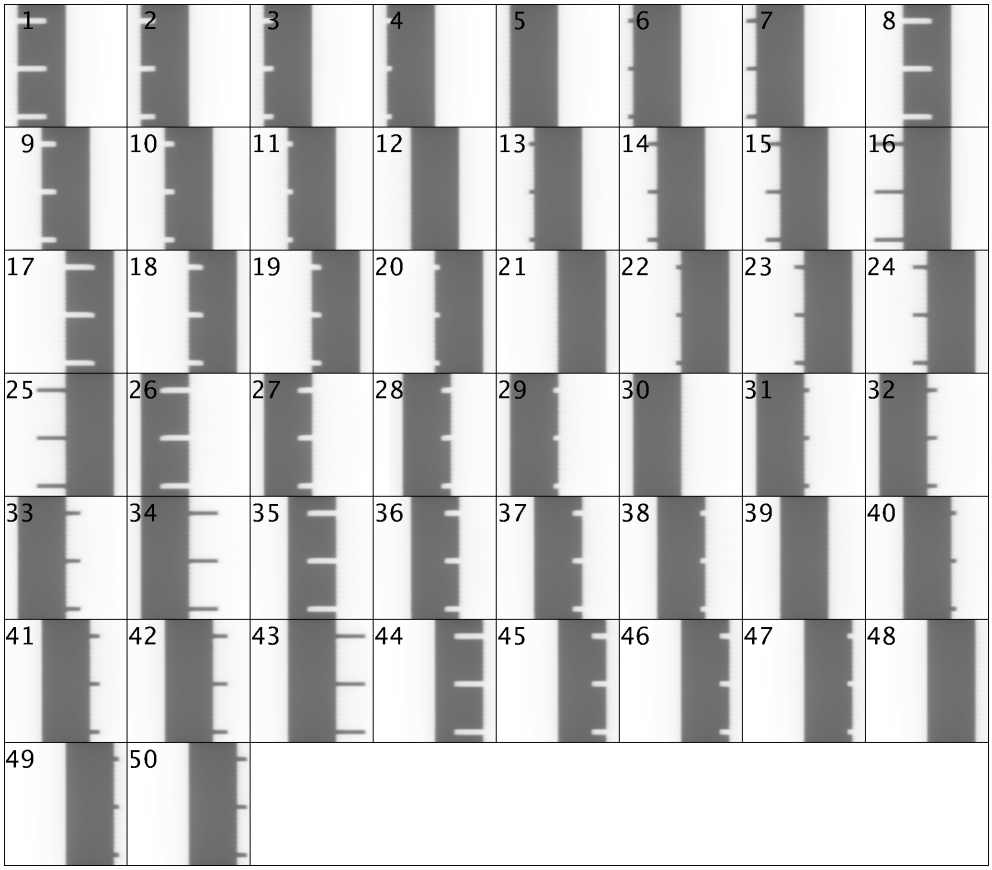

Fig. 2-6: Field shapes used in the performance test.

Table 2-1: Average error and 1 standard deviation in the MLC position of the test fields shown in Fig. 2-6.

Method	Left MLC Average +/- 1SD [mm]	Right MLC Average +/- 1SD [mm]
Threshold (45%)	-0.67 +/- 0.41	0.53 +/- 0.44
Threshold (50%)	-0.31 +/- 0.37	0.17 +/- 0.39
Threshold (55%)	0.03 +/- 0.35	-0.18 +/- 0.36
Threshold (60%)	0.36 +/- 0.36	-0.52 +/- 0.36
DOG Method	-0.09 +/- 0.15	-0.06 +/- 0.20

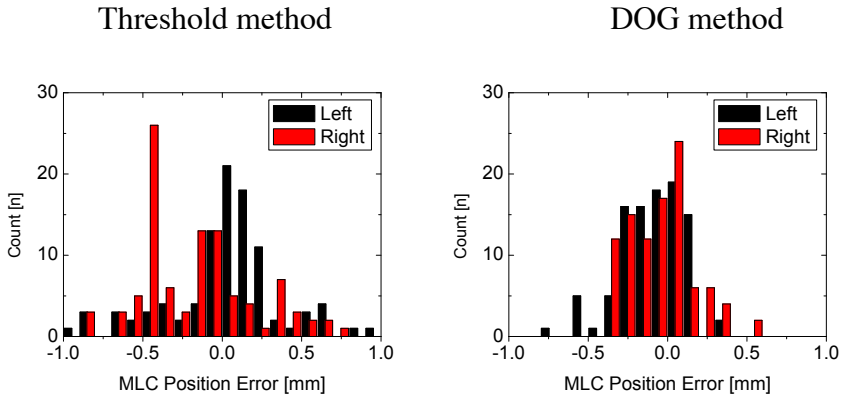

Fig. 2-7: Histogram of the multileaf collimator (MLC) position error (left: 55% threshold method; right: DOG method.

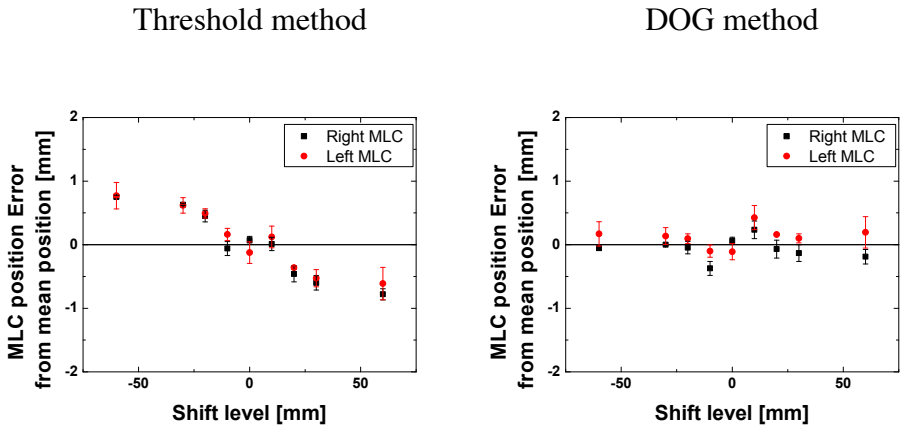

Fig. 2-8: Shift-level dependence for the threshold method (left) and DOG method (right).

2.2.4 Log data

The Elekta software protocol, iCom®, enables the digital accelerator to interface with third-party systems. Using this protocol, the log data, including cumulative MUs, MLC, jaw positions, and the corresponding gantry angle, were recorded via an RT Desktop controller (Elekta) during treatment. The sampling frequency was approximately 4 Hz. Slipping of the data sampling rarely occurred during low-dose rate irradiation.

The data format recorded in iCom® was converted to the beam data format in TPS using an in-house program. It would be enough to collect the data with this sampling interval in VMAT because the corresponding gantry angle is 1.5 degrees at maximum and the maximum gantry speed is 6 degrees/sec in Elekta Synergy.

2.3 Comparison of MLC position between log data and EPID detection

The verification of the log data was performed with the clinical data for 3 lung cancer patients. The dynamical MLC motion for VMAT was captured sequentially by EPID with an interval of 0.46 s. The MLC position inside the irradiated field was determined with the DOG algorithm. The corresponding log data was simultaneously recorded during treatment in each fraction for each patient.

Figure 2-9 shows the position of the left and right leaves in No. 20 and No. 21

(middle leaves) recorded in the log data (solid curves in upper part of each panel) and detected by the DOG method (square symbols in upper part of each panel) and its difference between the log data (solid curves in bottom part of each panel) and EPID detection for patients A–C. Since only 256 sequential images (meaning 256 × 0.46 = 117.76 s) were obtained in Elekta iViewGT, the data from a certain period of the middle range of the gantry angle obtained in EPID detection are missing in the figure. For other ranges, the agreement seems to be good. In Table 2-2, the difference between the log data and EPID detection for the 3 patients are summarized for each treatment day.

The difference between the log data and EPID detection was evaluated as,

$$d(i) = Position_{EPID}(i) - Position_{\log}(i), \tag{2-3}$$

$$\bar{d} = \frac{\sum_{i}^{n} d(i)}{n}, \tag{2-4}$$

$$SD = \sqrt{\frac{\sum_{i}^{n} \left(d(i) - \bar{d}\right)^2}{n-1}}, \tag{2-5}$$

where $\bar{d}$ is the average of difference, and SD is the standard deviation of the error. In this study, the maximum average value was 0.88 mm for the first day for patient C, whereas that of the standard deviation was 0.93 mm for the fourth day for patient B.

Patient A

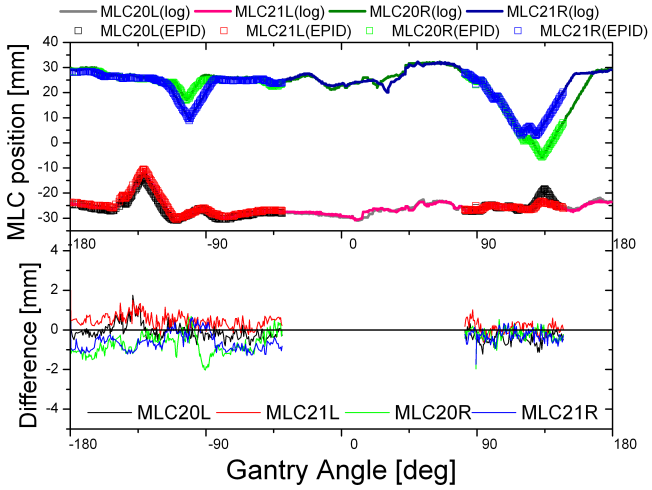

Patient B

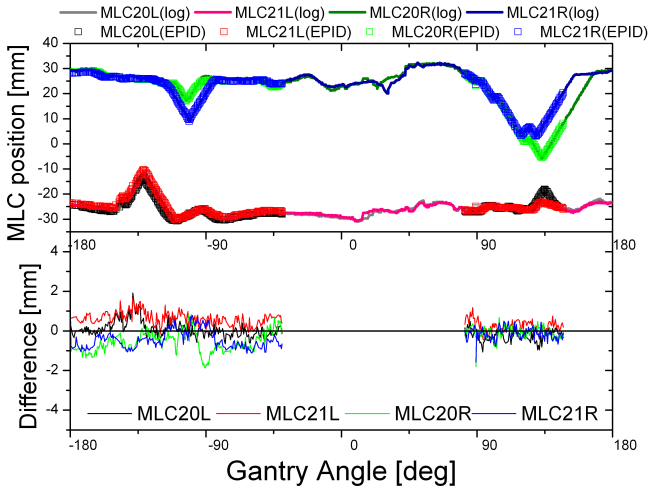

Patient C

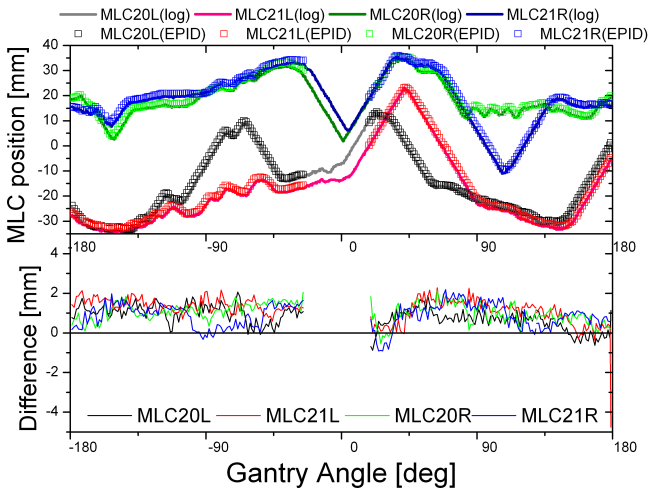

Fig. 2-9: Position of left and right leaves (No. 20 and No. 21) during a first-day treatment for 3 patients. The solid curves are those of log data, whereas the square symbols are those of EPID detection. The difference between the log data and EPID detection is also shown in the bottom of each panel.

Table 2-2: Average and 1 standard deviation in difference between the log data and EPID detection.

Patient A:

	data points	Left MLC		Right MLC		All MLC	
	[n]	Average [mm]	1SD [mm]	Average [mm]	1SD [mm]	Average [mm]	1SD [mm]
Day1	353	-0.01	0.48	-0.25	0.49	-0.13	0.50
Day2	355	0.15	0.49	-0.15	0.49	0.00	0.50
Day3	355	0.19	0.45	-0.06	0.47	0.06	0.48
Day4	354	0.23	0.46	-0.03	0.48	0.10	0.49

Patient B:

	data points	Left MLC		Right MLC		All MLC	
	[n]	Average [mm]	1SD [mm]	Average [mm]	1SD [mm]	Average [mm]	1SD [mm]
Day1	326	0.32	0.53	0.12	0.48	0.22	0.51
Day2	371	0.43	0.58	0.17	0.46	0.30	0.54
Day3	84	-0.03	0.37	-0.23	0.26	-0.13	0.34
Day4	242	0.26	0.93	0.10	0.58	0.18	0.78

Patient C:

	data points	Left MLC		Right MLC		All MLC	
	[n]	Average [mm]	1SD [mm]	Average [mm]	1SD [mm]	Average [mm]	1SD [mm]
Day1	242	0.88	0.60	0.88	0.55	0.88	0.57
Day2	242	0.40	0.53	0.37	0.56	0.39	0.55
Day3	232	-0.29	0.57	-0.29	0.60	-0.29	0.58
Day4	243	0.11	0.45	0.09	0.50	0.10	0.48

2.4 The uncertainty with use of log data

From the comparison with the EPID detection, the uncertainty of the log data was found to be less than 0.88 ± 0.93 mm in the MLC position. The EPID detection has an intrinsic error involved with the panel position and the performance of the detection algorithm. As described in 2.2.1, the 3-month reproducibility of the panel position showed that this was less than 0.4 mm. The performance test of the DOG algorithm also showed in 2.2.3 that the uncertainty due to the algorithm was negligibly small. Of course, the complex field shapes in clinical cases could result in degradation of the detection performance. The MLC position

significantly affects the dose distribution to the patient. An error of more than 2 mm can provide the dose distribution in the peripheral region of the target. In previous studies, several authors have investigated MLC detection methods with the threshold base [95] and gradient base [96, 97] for static irradiation. Gregory *et al*. [91] showed the susceptibility of uncertainty for dose delivery with VMAT irradiation; the average percent in differences of PTV Dmean values per mm bank shift using VMAT for head and neck and prostate plans were 1.2% per mm and 1.0% per mm, respectively. Since the VMAT plan in this study might be less sensitive than Gregory's plans, even a 1-mm MLC error does not result in a large dose difference.

Irradiation information detected by EPID is the most direct and reliable data, but there are some limitations with its use for dose calculation, including the limited number of image acquisitions, no gantry angle information, no jaw information, among others. The log data is convenient to use for the dose calculation since all of the data, such as the MLC and jaw position, MU, and gantry and collimator angles, are included in the log data. In Chapter 4, I will use the log data to reconstruct the 4D dose distribution to the patient.

3 Accuracy of the dose calculation with CBCT using the ROI mapping method

3.1 Introduction to Chapter 3

Visualization of the actual dose region delivered in a treatment is an interesting issue in radiation therapy. A rotational treatment, such as VMAT, together with an irradiation of kV beams can provide "in-treatment kV-CBCT" images, which include the information of anatomy localization during treatment [98, 99]. These technologies not only allow for correction of the internal target position errors, but also verify the "actually delivered" dose distribution. To obtain the actually delivered dose distribution, one needs to do dose calculation with CBCT. However, the current quality of a CBCT image is really poor in comparison with planning CT. In addition, the HU in CBCT has a location dependency in the reconstruction space, in which the magnitude of scattering artifacts is affected by the scanned object size [100, 101]. Furthermore, the reduction of a number of projections in 4D CBCT yields a severe streak artifact in comparison with that in 3D CBCT [84]. Therefore, for dose calculation with CBCT, some correction strategies are necessary [102 -104].

In this chapter, I introduce the ROI mapping method for dose calculation [81, 82]. This method assigns the density directly in each ROI contoured on the CT images. To evaluate the accuracy of the ROI mapping method, the benchmark test of the ROI mapping

method is performed using the planning CT. In Chapter 4, I will apply this method to 4D dose calculation using in-treatment CBCT.

3.2 Materials and methods for the evaluation of the ROI mapping method

3.2.1 Treatment planning

The ROI mapping method was examined using the treatment planning CT for three lung cancer patients. First was a primary lung cancer, and its histopathological type was adenocarcinoma. Second was suspected of primary lung cancer by CT scans, and there was no information of the pathology. The last was a metastatic lung cancer, and primary tumor was squamous cell carcinoma of the anal canal. Patient and tumor characteristics and treatment information are summarized in Table 3-1. The planning CTs were acquired by a 16-slice volumetric CT scanner (AquillionLB; TOSHIBA, Japan). All images were transferred to Pinnacle^3 V9.2 TPS (Philips, USA). The dose calculation was performed in the Pinnacle TPS using the collapsed-cone superposition convolution algorithm with an isotropic 3-mm dose grid resolution.

Table 3-1: Patient and tumor characteristics and treatment information

w	Age(y)	Sex	TNM	Tumor location	tumor size (mm)	tumor size (cc)	Pathology	Tumor Moving Distance (mm)			Treatment Time (sec)	MU
								x	y	z		
1	73	M	cT1aN0M0	Lt lower lobe	12	5.4	Adeno	0.0	1.8	12.7	235	1896
2	87	M	cT1aN0M0	Lt upper lobe	17	6.7	No Info	0.9	0.8	2.3	210	2180
3	77	F	M1	Rt lower lobe	14	8.3	No Info	1.7	1.6	9.7	197	1700

Abbreviations: Adeno, Adenocarcinoma; No Info, No Information of the pathology

3.2.2 Original plan

In the original planning, the dose distribution was calculated with the calibration table of planning CT number to physical density (CT-to-density table), which was obtained with a tissue characterization phantom (Model 467; Gammex, USA). Using the CT-to-density table, the dose calculation takes the density heterogeneity into account with voxel-by-voxel of the CT.

3.2.3 ROI mapping method

In contrast to the original plan, the ROI mapping method does not assign the density from the CT-to-density table, but manually assigns a density for each ROI. The procedure of the ROI mapping method is described below.

(1) The ROIs for all structures on the CT were segmented, and then, the mean HU number values were evaluated for each ROI.

(2) The HUs in each ROI were overridden uniformly with these mean HU values.

(3) The CT-to-density table was applied.

Thus, a uniform density is assigned for each ROI. This method is very effective in the dose calculation on CBCT image [107] if the planning CT is acquired in advance because the ROI density on CBCT is replaced with the mean density of the corresponding ROI on the planning

CT. In this chapter, I apply the ROI mapping method to the planning CT and evaluate the accuracy of this method by comparing it with the original plan.

3.2.4 ROI creation

Five ROIs were created for this study: bone, lung, airway, soft tissue, and ITV. For creating the ROI for bone and soft tissue, a threshold of 100 to 3000 HU and -200 to 100 HU were respectively applied, whereas for the lung ROI, the organ model tool in the Pinnacle was applied. The GTV was delineated by the radiation oncologist using the lung window (window: 1600 HU; and level: -1300 HU).

3.2.5 Evaluation

The original treatment plans of each patient were transferred to the ROI-mapped CT so as to reproduce the same beam settings as in the original plan. Then, the dose calculation was performed. Dose differences between the ROI mapping method and the original plan were analyzed with the dose-volume histogram (DVH) and the dose indices, such as the minimum, maximum, and mean doses of GTV, along with doses at the isocenter and at the center of the GTV.

3.3 Results

Table 3-2 shows the mean HU and the corresponding mean density values for the bone, lung, airway, soft tissue, and ITV of the 3 patients. Each structure provided a similar mean density value for each patient. The density of the ITV was much smaller than that of the

soft tissue because this region includes the GTV and a part of the lung. In principle, the density of the ITV can depend on tumor motion; the larger the amplitude of tumor motion, the smaller mean density for the ITV.

The comparison of the dose distribution between the original plan (left panels) and the ROI mapping method (right panels) for patients 1–3 are shown in Figs 3-1–3-3. There, top and middle panels show the density distribution and dose distribution, respectively. The left-bottom panel shows the DVH, where the solid curves indicate the DVH for the original plan, while the dashed ones indicate the DVH for the ROI mapping method. The right-bottom panel is an enlargement. The dose distributions of the ROI mapping method and the original plan are very similar to each other, and the DVH curves of the ROI mapping method are in good agreement with those of the original plan. This can also be seen in Table 3-3, where dose differences for the minimum, maximum, and mean doses of GTV, and doses at the isocenter and at the center of the GTV between the ROI mapping method and the original plan are indicated. For these indices, the maximum dose difference was only 1.2% in the center of the GTV for patient 3.

Table 3-2: Mean HU values and corresponding density values for the bone, lung, airway, soft tissue, and ITV of 3 patients

No.	Bone		Lung		Airway		Soft tissue		ITV	
	CT value (HU)	Density (g/cc)	CT value (HU)	Density (g/cc)	CT value (HU)	Density (g/cc)	CT value (HU)	Density (g/cc)	CT value (HU)	Density (g/cc)
1	340.0	1.210	-703.0	0.314	-801.6	0.209	-30.7	0.989	-497.0	0.533
2	430.9	1.254	-745.1	0.269	-965.7	0.004	-1.9	1.016	-237.0	0.763
3	269.7	1.176	-744.6	0.269	-766.8	0.246	-2.1	1.000	-451.8	0.579

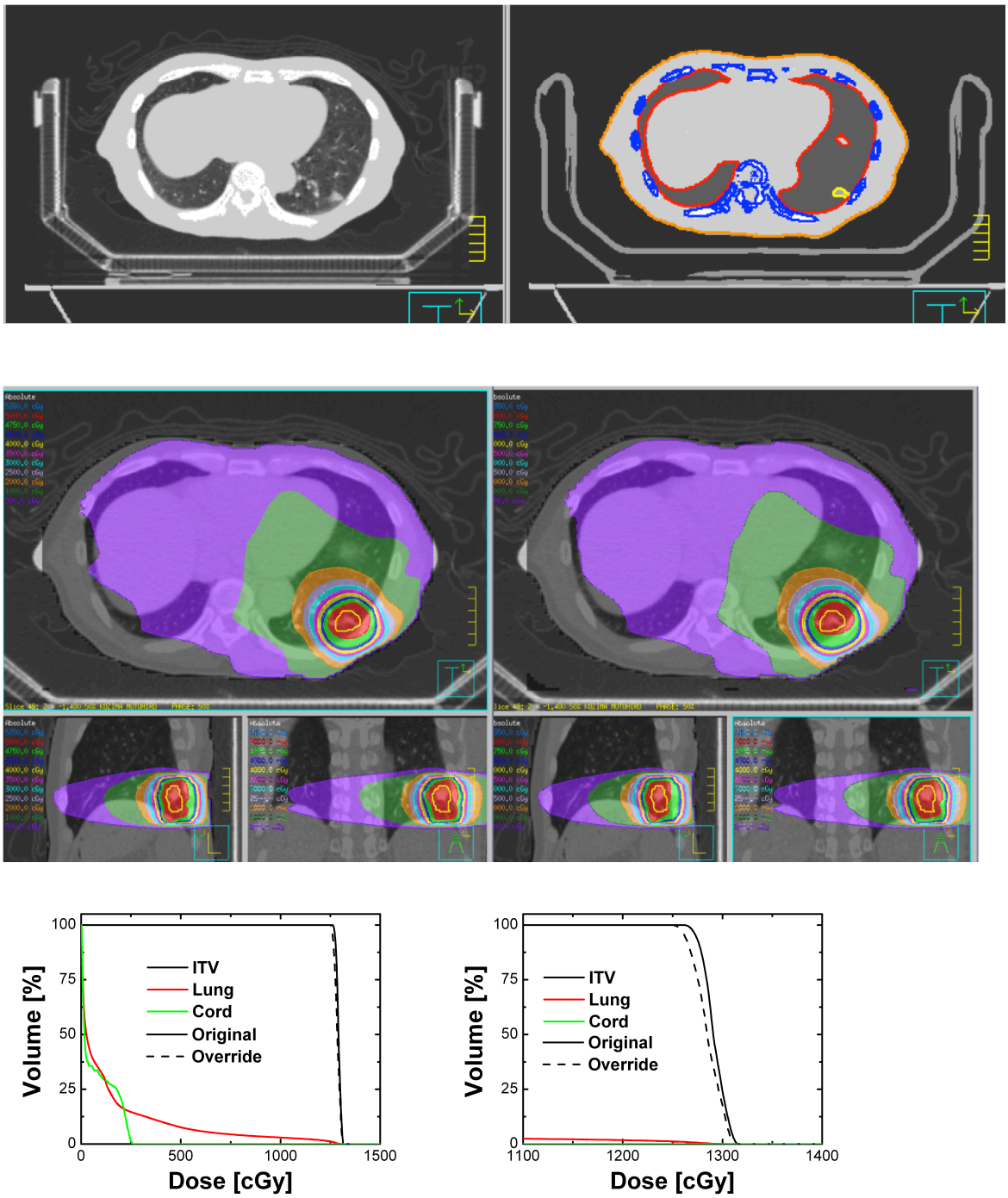

Fig. 3-1: Comparison of the dose distribution between the original plan (top- and middle-left panels) and ROI mapping method (top- and middle-right panels) for patient 1. The left-bottom panel shows the DVH, where the solid curves represent the DVH for the original plan, while the dashed curves represent the DVH for the ROI mapping method. The right-bottom panel is its enlarged display.

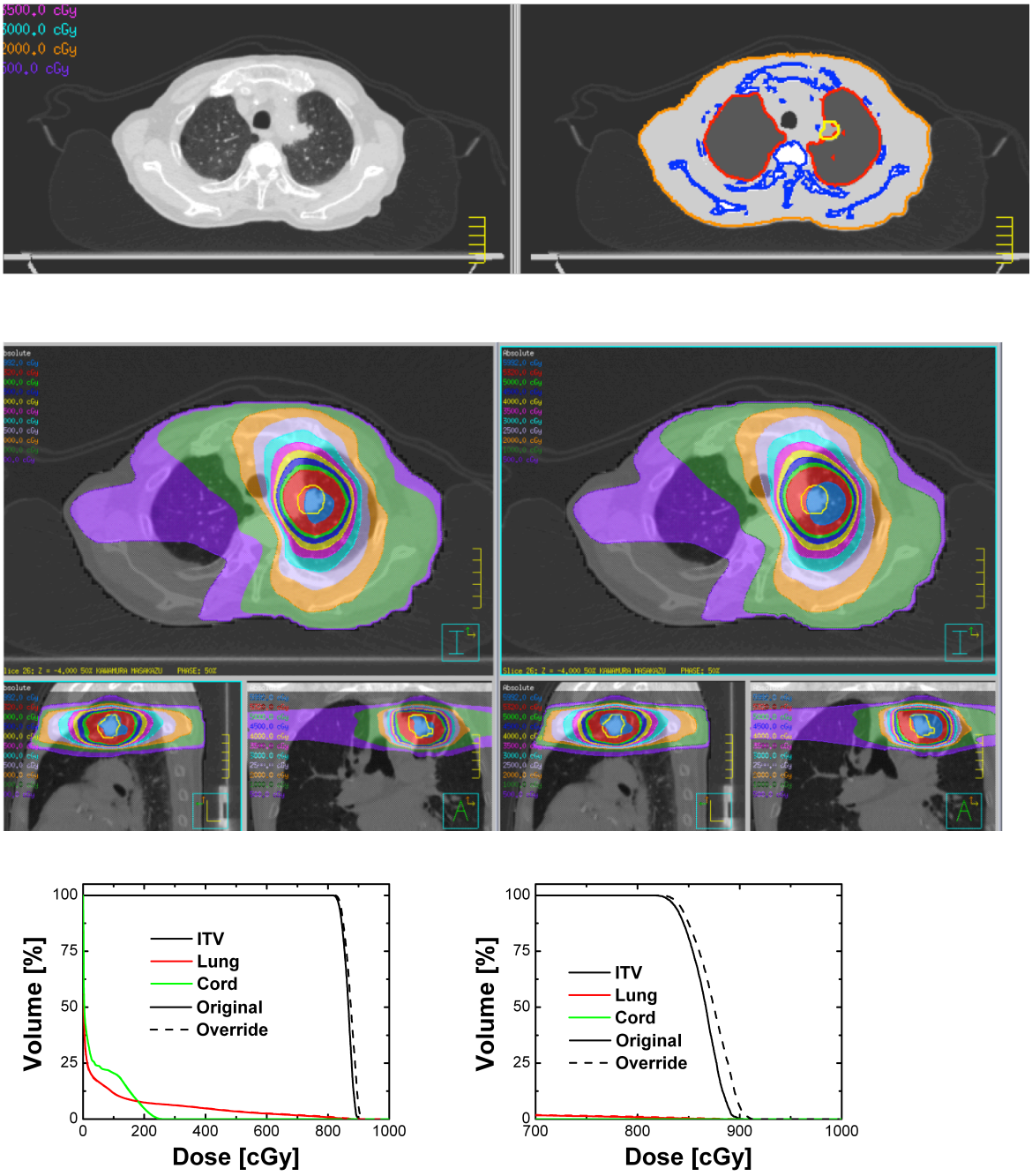

Fig. 3-2: Comparison of the dose distribution between the original plan (top- and middle-left panels) and the ROI mapping method (top- and middle-right panels) for patient 2. The left-bottom panel shows the DVH, where the solid curves indicate the DVH for the original plan, while the dashed ones indicate the DVH for the ROI mapping method. The right-bottom panel is its enlarged display.

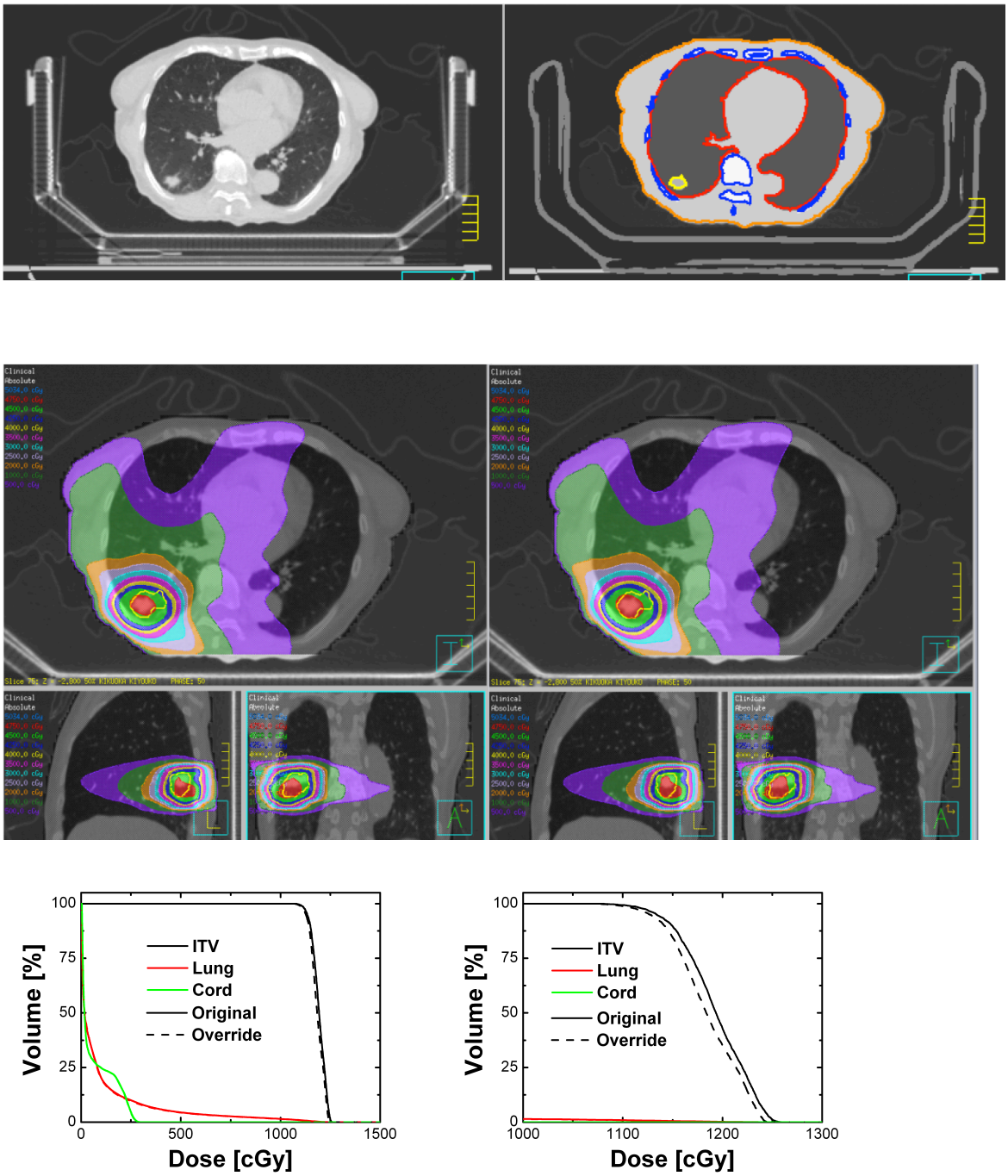

Fig. 3-3: Comparison of the dose distribution between the original plan (top- and middle-left panels) and the ROI mapping method (top- and middle-right panels) for patient 3. The left-bottom panel shows the DVH, where the solid curves indicate the DVH for the original plan, while the dashed ones indicate the DVH for the ROI mapping method. The right-bottom panel is its enlarged display.

Table 3-3: Dose difference between the ROI mapping method and the original plan.

No.	Isocenter		Center of GTV		GTV minimum		GTV maximum		GTV mean	
	[cGy]	[%]	[cGy]	[%]	[cGy]	[%]	[cGy]	[%]	[cGy]	[%]
1	5.5	0.4	7.0	0.6	7.7	0.6	5.1	0.4	5.0	0.4
2	-2.9	-0.3	-2.5	-0.3	10.3	1.3	9.1	1.0	4.4	0.5
3	11.0	0.9	13.8	1.2	12.5	1.2	12.3	1.0	11.4	1.0

3.4 Discussion

The ROI mapping method can reproduce the dose distribution in the original plan, for which the dose calculation takes the density heterogeneity into account in voxel-by-voxel of the CT using the CT-to-density table. Appling the ROI mapping method to the same planning CT as in the original plan for 3 lung cancer patients, I have demonstrated the accuracy of the ROI mapping method within 1.2% at most. This accuracy brings the dose calculation on the ROI mapping CBCT.

In previous studies, in contrast, Yang *et al*. and Tucking *et al*. [108, 109] showed that the dose difference between CBCT and the planning CT would be more than 5% when using the CT-to-density table directly generated by the phantom . Several authors have investigated the suitability of CBCT for dose calculation and developed different pixel correction strategies depending on the CBCT system properties [109-116]. The ROI mapping method was first introduced by Hu *et al*. and Richter in order to calculate the dose distribution

using CBCT images [105, 106]. Although they did not show the benchmark test using the planning CT, the validity of this method was strongly supported by the present result.

The advantage for using the CBCT image in the dose calculation is that the day-by-day position and shape of the body and anatomies are taken into account automatically. However, for the application of the ROI mapping method to CBCT images, it should be noted that the difference in the structure segmentation between the planning CT and CBCT yields additional inaccuracy in the dose calculation. I will discuss this in more detail in Chapter 4.

4 4D dose calculation using 4D-CBCT and log data

4.1 Introduction to Chapter 4

As described in the introduction, there are some challenges in using IMRT with regard to a moving target and other organs. Clearly, if a movement occurs between delivery of any of the IMRT fields, the dose may not add up to the desired total dose as planned [117]. If there is organ movement during the delivery of a single IMRT field, the delivered intensity and dose map can also be very different from the planned one. This is known as the "interplay effect".

The effects of motion on IMRT delivery have been studied by many authors [118-128]. Bortfeld *et al*. [120] predicted that the interplay effect would, for the most part, average out with a large number of fractions. However, this is not the case with a hypo-fractionated radiosurgery-type course of treatment (1–5 fractions). In addition, there are substantially fewer studies of the interplay effect in VMAT [120, 122, 126, 127], particularly for hypo-fractionated dose regimens. Especially of note, there is no study attempting to reconstruct the dose distribution using only data acquired during treatment.

In Chapter 2, I demonstrated that the MLC position recorded with LINAC log data was reproduced well compared to the actual treatment. In addition, in Chapter 3, the accuracy of the dose calculation using the ROI mapping method was evaluated with the planning CT. With these methods, in this chapter, I reconstruct the actual dose distribution for in-treatment

4D CBCT. The dose distribution with the present calculation was based on projection images and log data acquired during VMAT delivery and includes the interplay effect. The reproducibility of the treatment plan for a moving target in lung cancer patients is then discussed.

4.2 Materials and methods for 4D dose calculation

In this section, the materials and methods for the 4D dose calculation are described. The workflow of 4D dose calculation in the present study is shown in Fig. 4-1. The 4D dose was evaluated with the actual LINAC parameters on in-treatment 4D CBCT, which was reconstructed by the kV-projection images acquired during VMAT treatment. The LINAC parameter was synchronized with the kV-projection images through the gantry angle.

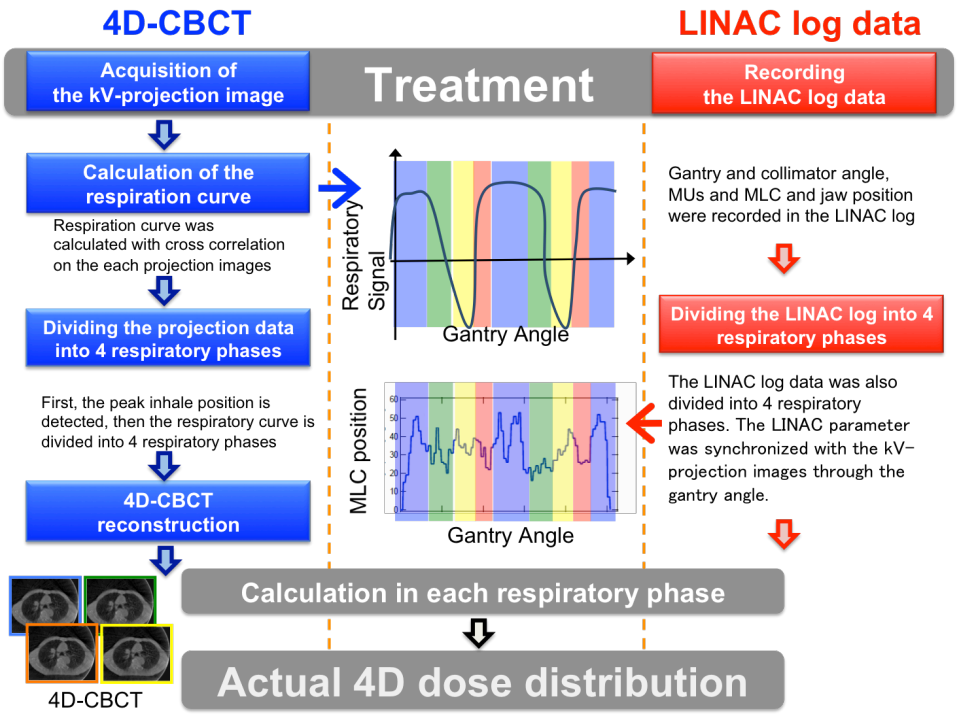

Fig. 4-1: The workflow of 4D dose calculation in the present study.

4.2.1 Respiratory signal acquisition and 4D CBCT reconstruction

The cone-beam projection images were acquired during VMAT delivery using an on-board kV X-ray imager, XVI (Elekta, UK). The kV projection image was acquired by a flat panel imager operating at a resolution of 512 × 512 pixels, with a pixel size of 0.52 mm at the isocenter and at a fixed frame rate of 5.5 fps. There are three types of collimators, S, M, and L types. They allow for the reconstruction of small, medium, and large fields of view, respectively. With S collimator cassettes, the center of the kV radiation field was in line with the central axis of the kV X-ray unit. With M and L collimator cassettes, the kV radiation field was offset in the cross-line direction by 11.5 and 19 cm, respectively, at the imaging panel. For the present study, all kV images were acquired with use of a beam of 120 kVp, 40

mA/40 ms with an M collimator at an axial field length of 20 cm.

The radiation dose received by CT scanners is generally evaluated by CT dose index (CTDI). The measured CTDI value in pre-4D CBCT scan was 12.6 mGy under clinical condition using a calibrated ion chamber, which is about 0.1% of the prescribed dose in 4 fractionated lung SRT. It was realized that an extra dose from kV X-ray was very low compared with dose from MV X-ray and the verification of the organ motion during treatment was more benefit than additional receiving a relatively small amount dose.

The patient respiratory phase was determined from kV projection images using an in-house phase recognizing software based on normalized cross correlation (NCC) [130]. This method implements NCC between adjacent kV projections in a limited region. The respective segments are shifted along the cranio-caudal axis on the next projection image in the search for the maximum value of NCC, using the segments on previous projection images. Finally, a low periodic component caused by the gantry rotation and high component caused by noise were removed by a band pass filter. Thus, a signal concerned with respiration was obtained by displacement of the cranio-caudal direction.

In this study, the in-treatment 4D CBCT images were reconstructed by dividing the projection images into 4 phase bins. An in-house program based on the algorithm developed by Feldkamp, Davis, and Kress, and by Webb was used. In order to use this for dose

calculation, the reconstructed size was as large as possible (500 mm × 500 mm × 120 mm with 1 mm voxel cubic, for lateral, vertical, and longitudinal directions, respectively).

4.2.2 SRT-VMAT planning for lung cancer

The patients selected in this study were the same as in Chapter 3 (Table 3-1). The PTV for the lung tumor was created with a 5-mm margin of internal target volume generated from 10 4D CT sets using a 16-slice volumetric CT scanner (AquillionLB; TOSHIBA, Japan). Patients 1 and 3 received a D95 prescription of 50 Gy for PTV in 4 fractions, whereas patient 2 received a D95 prescription of 56 Gy for PTV in 7 fractions. The single-arc VMAT with 6 MV was created by SmartArc in the Pinnacle^3 v9.2 treatment planning system (Philips, USA). Through the planning CT acquisition and course of treatment, a stereotactic body frame was used for constraint of respiratory motion. The constraint on MLC motion of 0.1 cm/degree was applied in the VMAT inverse plan so that MLC had little chance to hide the PTV, done in accordance with the protocol in The University of Tokyo Hospital. The calculation was based on 3D calculation.

4.2.3 Data acquisition of LINAC parameters

The data acquisition of LINAC parameters was performed by using iCom® (Elekta, UK), which was described previously (see Section 2.2.3). The data was acquired through a course of treatment for the 3 patients. The sampling number is dependent on the delivery time.

In this study, the delivery time was 235 (patient 1), 180 (patient 2), and 197 (patient 3) sec, which corresponded to 791, 652, and 731 samplings, respectively.

4.2.4 ROI mapping

Daily CBCT may be convenient for 3D dose verification of the dose delivered to a patient after each treatment. As described in Chapter 3, however, the artifacts in CBCT, mainly caused by the scattering and hardening of the kV X-ray spectrum, are much worse in comparison with the artifacts of the planning CT; the HU in CBCT is substantially unreliable. The situation is worse in its 4D version, in which the streak artifact appears because of the reduction of number of the projection images in each phase. Such image degradation affects the accuracy of dose calculation. Therefore, to avoid this, a patient-specific ROI mapping method, described in the previous chapter, was applied. In this method, the relative densities in the anatomical regions defined by ROI contouring were measured by means of the planning CT. Then, these densities were substituted into the corresponding anatomies delineated in 4D CBCT. The 5 regions of the lung, airway, water (including fat and muscle), bone, and ITV were considered. In Table 3-2 of the previous chapter, these mean values are indicated.

4.2.5 4D dose reconstruction

The dose distribution was reconstructed using in-treatment 4D CBCT and LINAC

log data, as illustrated in Fig. 4-1. The process was as follows:

(1) The kV cone-beam projection images and the LINAC parameters from iCom® were acquired during VMAT delivery.

(2) The respiratory signal was derived from the cone-beam projection images.

(3) Based on the respiratory signal, the projection images and LINAC parameters were classified into 4 respiratory phases.

(4) The 4D CBCT sets (4 respiratory phases) were reconstructed.

(5) The beam data form of Pinnacle TPS was created from the LINAC parameters in each phase. Thus, 4-beam data sets corresponding to the 4D CBCT sets were produced in each treatment fraction. These beam sets were sent to Pinnacle TPS.

(6) The image region of the 4D CBCT was extended to 700 mm × 700 mm × 500 mm in lateral, vertical, and longitudinal directions, respectively, so as to include a stereotactic body frame in the calculation region.

(7) The 4D CBCT sets were converted to DICOM format and sent to Pinnacle TPS. Then, the ROIs (GTV, lung, cord, airway, and soft tissue) were delineated in each phase.

(8) The dose calculation was performed in Pinnacle TPS with 3-mm resolution. The patient-specific ROI mapping method was applied.

Since the corresponding actual beam information to the acquisition time of the projection

images was used for the dose calculation in each phase of in-treatment 4D CBCT, absolute dose distribution was reconstructed by using only the data.

4.2.6 Validation of the 4D dose calculation

For validation of the present 4D dose reconstruction method, a measurement using the moving phantom, QUASAR (MODUS Medical Inc.), was performed (Fig. 4-2). The moving insert consists of the wood material mimicking lung with 6 cm diameter, and the spherical polyethylene material mimicked tumor with 3 cm diameter (considered as GTV). The insert was controlled with 2.0 cm amplitude and a 4-sec period. A pinpoint ion chamber (TM31014, PTW, Freiburg) was inserted in the center of the spherical polyethylene material.

A single-arc VMAT test plan, which provided the rapid leaf motion with 490 MUs, was selected to validate the proposed method. Dose measurements were performed with both a stationary and moving target. The calculated dose was compared with the measured dose at the center of the GTV. In this phantom study, the dose calculation was performed on not the in-treatment CBCT but on the planning CT images acquired during the planning 4D CT scan, because there was no need to consider geometrical changes of the object.

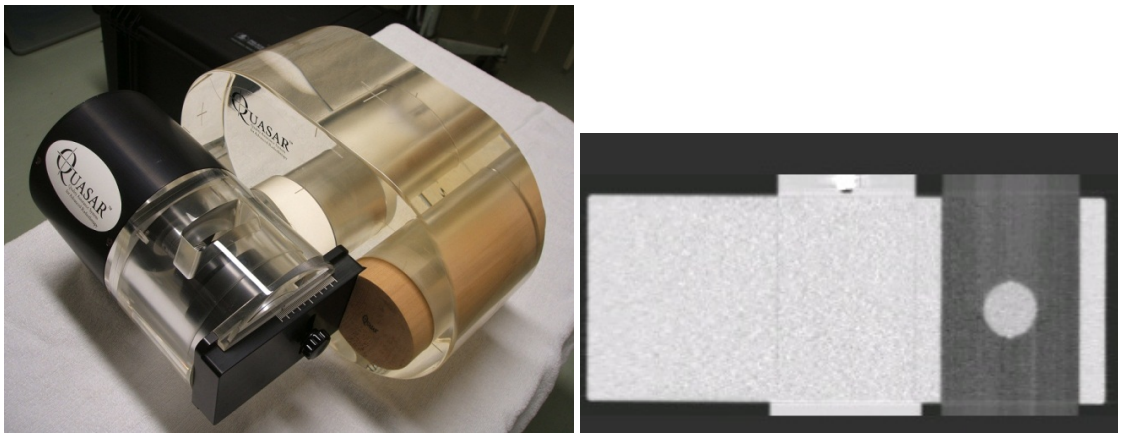

Fig. 4-2: Moving phantom used in this study (QUASAR [MODUS Medical Inc.]). The left panel shows the computed tomography (CT) image in coronal view. The moving insert consists of wood material, which mimicked lung with 6 cm diameter, and spherical polyethylene material, which mimicked tumor with 3 cm diameter.

4.2.7 Dose evaluation for patients

For comparison, the 3D dose calculation using in-treatment 3D CBCT and LINAC log data was performed in addition to the 4D dose calculation. The results of the 3D and 4D dose calculation were compared with that of the treatment plan.

In the treatment plan, the 3D dose calculation was performed. The target was to be confined in the ITV, and the prescription was to be delivered to the ITV as uniformly as possible. Therefore, I compared the mean, maximum, and minimum doses in the ITV for each fraction of each patient in the 3D dose reconstruction. On the other hand, the ITV could no longer be defined in the 4D dose calculation because the calculation was done in each phase independently. In principle, it is impossible to compare the dose distribution in each phase directly with that of the treatment plan, since the treatment plan calculates only a single phase.

Nevertheless, it would be useful to confirm the location of the hot and cold spots with the actual target location and shape. In the present study, the mean, minimum, and maximum doses for 4D dose calculation were evaluated by the summation of the phase as,

$$D_{mean\,4D} = \sum_{phase} D_{mean\,4D}(phase) \tag{4-1}$$

$$D_{\min\,4D} = \sum_{phase} D_{\min\,4D}(phase) \tag{4-2}$$

$$D_{\max\,4D} = \sum_{phase} D_{\max\,4D}(phase) \tag{4-3}$$

and those in the GTV were compared with those in the ITV of the 3D calculation, as well as those of the treatment plan. It is noted that the minimum and maximum doses in the 4D dose calculation did not correspond to the actual ones because the minimum and maximum dose points in the respective phases cannot equal each other. If the target was static, the minimum and maximum dose in 4D dose calculation would be exactly the same as both the actual and 3D doses.

4.3 Results

4.3.1 Phantom study

A VMAT test plan with a total 490 MUs were delivered to the QUASAR phantom. Without target motion, the reproducibility of the dose at the center of target (corresponding to the isocenter) was less than 0.2% for 3 sequential measurements. Then, the dose measurement for a moving target was conducted 3 times with simultaneous irradiation of the kV cone beam.

The beam delivery information was linked with the motion (namely, the respiratory signal) by synchronizing the kV imaging with the log data. Figure 1 shows the MU values assigned into each respiratory phase for 4D dose calculation.

The dose calculations with a single phase (i.e. 3D), 4 phases, and 10 phases were compared with the measurements in Fig. 4-2, which shows the relative dose difference at the center of the GTV with and without motion. Here the calculated dose was normalized to the measurement dose without motion ("Stationary" indicated in horizontal axis). Doses in each phase were obtained by using the planning CT for corresponding phase and log data, and the total dose was calculated by summing up the dose in each phase. Obviously, the measurement dose for a moving target was not in agreement with the 3D dose calculation, but it was in good agreement with the 4D dose calculation. In addition, the 4-phase 4D calculation well reproduced the measurements performed with the 10-phase calculation.

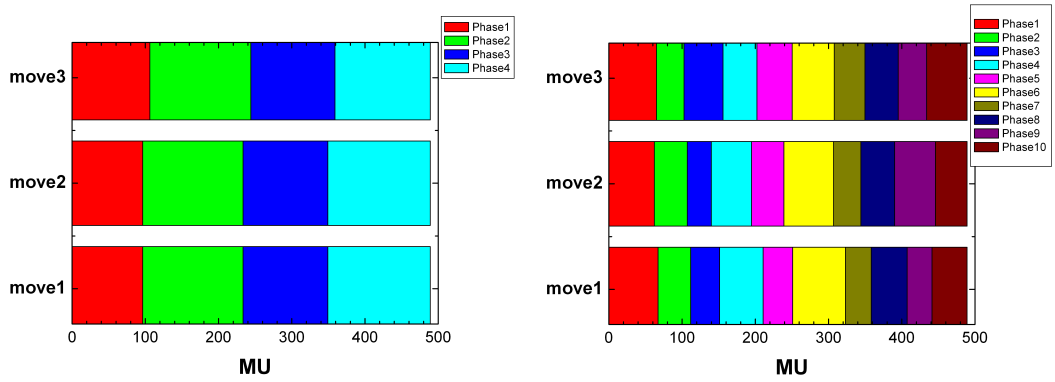

Fig. 4-3: Monitor unit (MU) values divided into 4 (left panel) and 10 (right panel) phases.

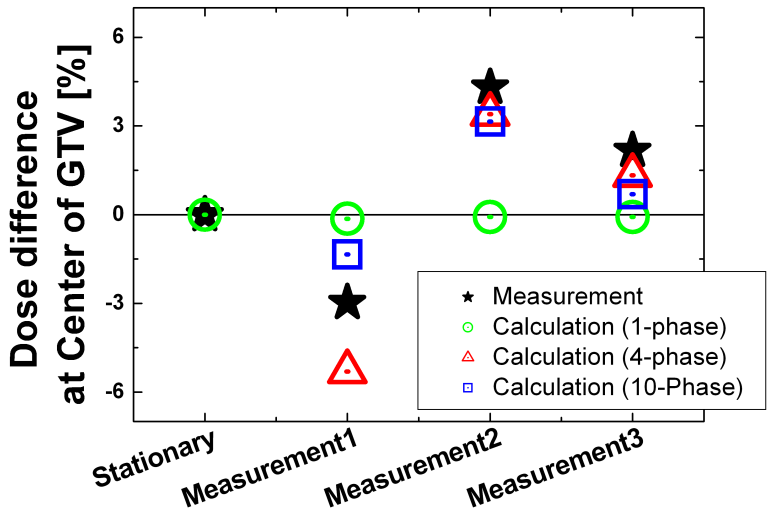

Fig. 4-4: Relative dose difference at the center of target with and without motion using the QUASAR phantom. Here, the calculated dose was normalized at the measurement dose without motion ("Stationary" indicated in horizontal axis).

4.3.2 Patient study

a) 3D dose calculation

In this subsection, I show the result of the 3D dose reconstruction using log data

and in-treatment CBCT for 3 lung cancer patients. Figure 4-5 shows a comparison of the 3D dose distribution between the treatment plan (left) and the actual treatment on the first day for patient 1 (right) on the isocenter plane. The yellow contour denotes the ITV contoured on respective CTs. The shape and location of the ITV on the isocenter plane seem to differ from each other.

Table 4-1: Dose at isocenter, mean, minimum, and maximum doses for the ITV. Dose differences between the treatment plan and each treatment fraction by 3D calculation are shown as a percentage.

Patient 1:

Index	Isocenter		mean		maximum		minimum	
	dose [cGy]	difference[%]	dose [cGy]	difference[%]	dose [cGy]	difference[%]	dose [cGy]	difference[%]
Plan	1298.7		1299.1		1315.8		1271.6	
Day1	1286.3	-1.0	1282.9	-1.2	1301.9	-1.1	1255.5	-1.3
Day2	1291.8	-0.5	1274.4	-1.9	1308.4	-0.6	1181.2	-7.1
Day3	1283.3	-1.2	1271.3	-2.1	1297.7	-1.4	1232.8	-3.1
Day4	1285.1	-1.0	1267.4	-2.4	1295.0	-1.6	1212.1	-4.7

Patient 2:

Index	Isocenter		mean		maximum		minimum	
	dose [cGy]	difference[%]	dose [cGy]	difference[%]	dose [cGy]	difference[%]	dose [cGy]	difference[%]
Plan	885.8		869.2		903.4		810.9	
Day1	870.9	-1.7	859.2	-1.1	907.7	0.5	800.1	-1.3
Day2	883.3	-0.3	867.7	-0.2	904.5	0.1	815.4	0.6
Day3	883.5	-0.3	877.1	0.9	918.4	1.7	819.4	1.0
Day4	881.1	-0.5	868.1	-0.1	910.1	0.7	808.5	-0.3
Day5	888.4	0.3	882.2	1.5	920.0	1.8	820.3	1.2
Day6	884.8	-0.1	879.2	1.2	915.0	1.3	823.3	1.5
Day7	883.5	-0.3	878.1	1.0	915.4	1.3	824.6	1.7

Patient 3:

Index	Isocenter		mean		maximum		minimum	
	dose [cGy]	difference[%]	dose [cGy]	difference[%]	dose [cGy]	difference[%]	dose [cGy]	difference[%]
Plan	1213.7		1175.4		1246.4		1068.5	
Day1	1198.7	-1.2	1159.0	-1.4	1235.1	-0.9	984.8	-7.8
Day2	1194.0	-1.6	1178.4	0.3	1235.4	-0.9	1039.4	-2.7
Day3	1196.4	-1.4	1180.9	0.5	1240.7	-0.5	1086.9	1.7
Day4	1200.7	-1.1	1184.4	0.8	1245.7	-0.1	1012.1	-5.3

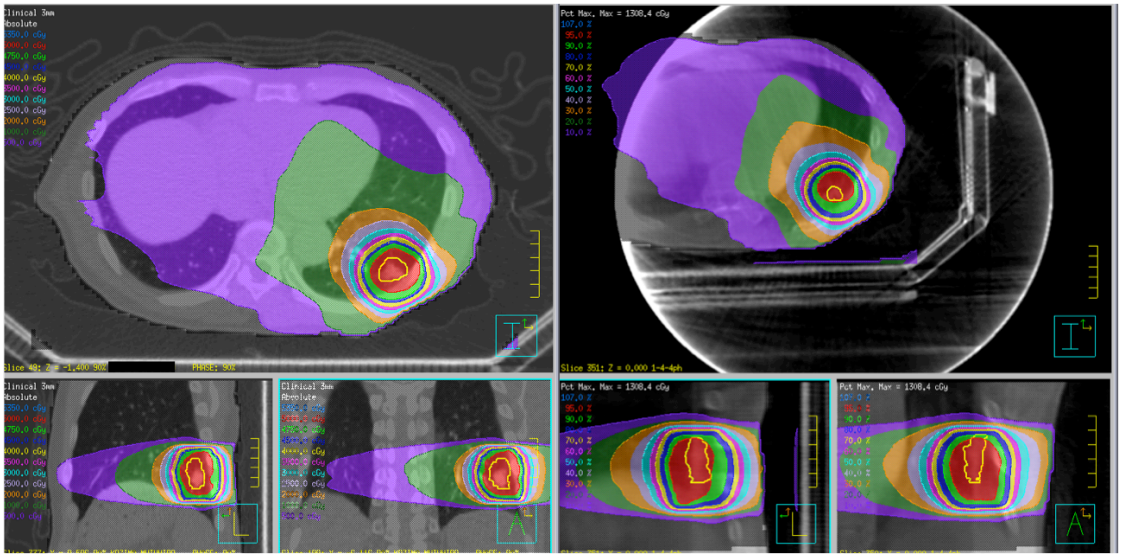

Fig. 4-5: Comparison of dose distribution between the treatment plan (left) and the actual treatment (3D) on the first day for patient 1 (right). The yellow contour in both images denotes the internal target volume (ITV).

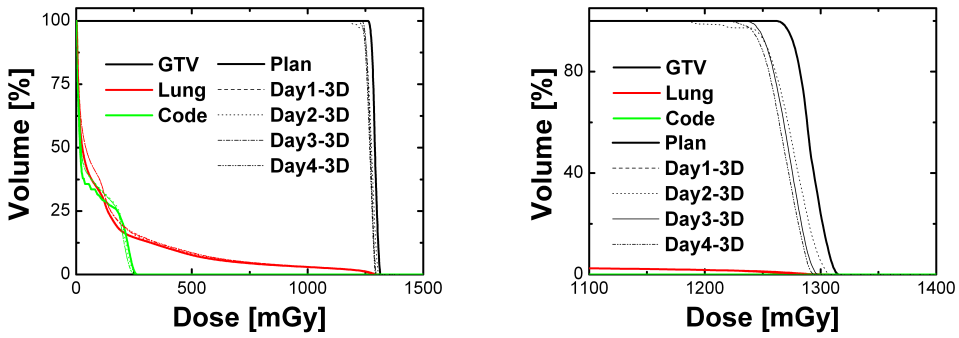

Fig. 4-6: Dose-volume histogram (DVH) comparison for patient 1. The solid curves indicate the DVH for the original plan while the dashed, dotted, dotted-dashed, and 2-dotted dashed lines indicate the DVH for the first, second, third, and fourth treatment

The dose calculation using in-treatment CBCT was performed with the ROI mapping method, described in Chapter 3. Figure 4-6 shows an example of a day-by-day comparison of DVH for patient 1. All DVH curves for the actual treatment were slightly different from those for the treatment plan. In Table 4-1, the dose differences at the isocenter, mean, minimum, and maximum doses for the ITV with 3D calculation are summarized. For all 3 patients, the dose in the ITV tended to be low compared with the planning dose. However, its variation with regard to the treatment day was not as great. The minimum dose in the ITV was somewhat different from that of the treatment plan. In particular, a more than 3% difference was observed at the second, third, and fourth days for patient 1, and the first and fourth days for patient 3.

b) 4D dose calculation

Four dimensional dose calculations for the same patients in the previous subsection were performed in the same manner as in the phantom study, except for the use of the in-treatment 4D CBCT. Examples of the dose distribution in each phase are shown in Fig. 4-7 (see Appendix C for the details of doses for each phase).

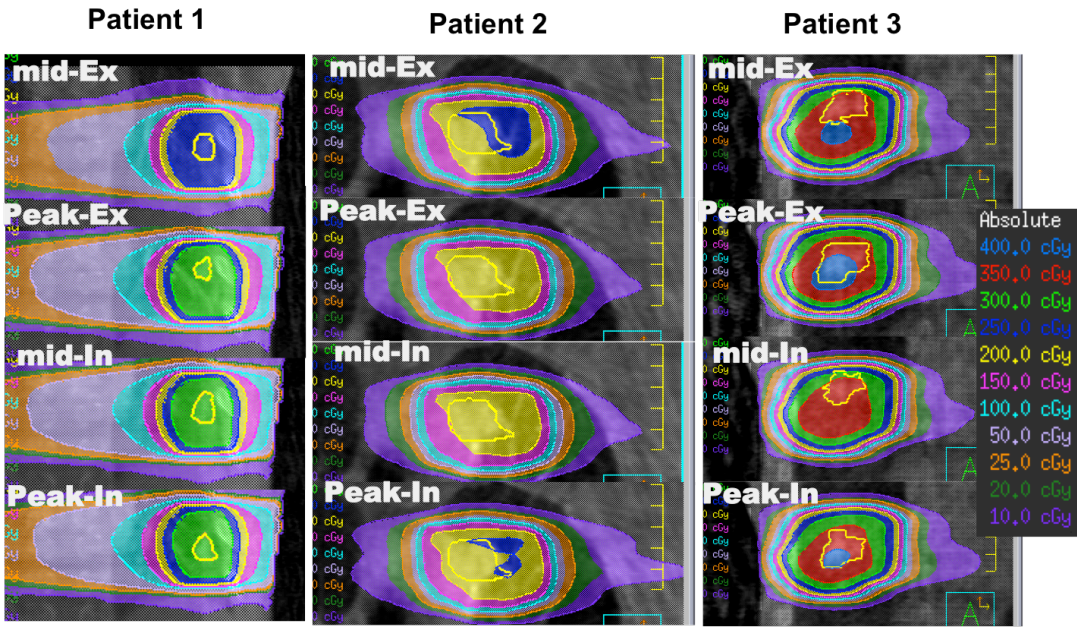

Fig. 4-7: Dose distributions in each phase at the first fraction for 3 patients (coronal view). The yellow contour in each image indicates the GTV.

Figure 4-8 shows the mean, minimum, and maximum doses in the GTV for patients 1–3, respectively. There, for comparison, the mean, minimum, and maximum doses in the ITV for the 3D calculation described in the previous subsection and the treatment plan are also shown. The square boxes represent the absolute mean dose, and the error bars represent the minimum and maximum dose. Black symbols indicate the dose indices from the 3D calculation, whereas red symbols indicate the dose indices from the 4D calculation. The fluctuation of the actual delivered dose in the treatment days was determined with both 3D and 4D calculation. In addition, a difference in the minimum dose between the 3D and 4D dose calculations was clearly observed on the second treatment day for patient 1, and on the first and fourth treatment days for patient 3.

Patient 1

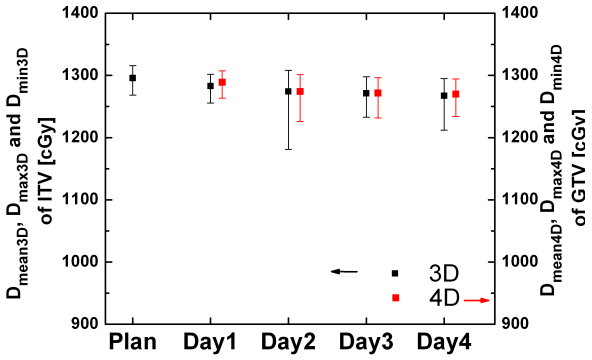

Patient 2

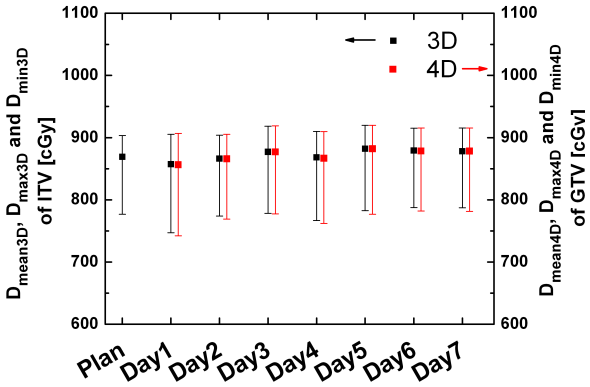

Patient 3

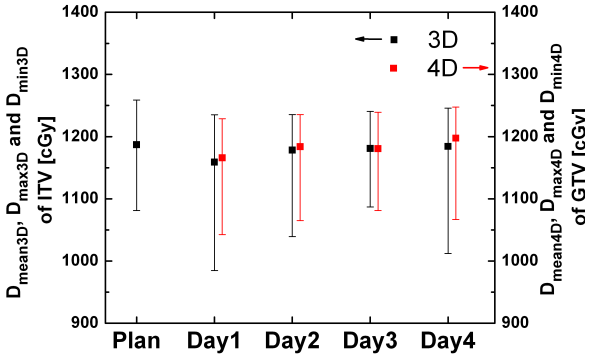

Fig. 4-8: Comparison of the mean, minimum, and maximum doses in the internal target volume (ITV; 3D) and the gross tumor volume (GTV; 4D). The square boxes represent the absolute mean dose and error bars represent the minimum and maximum dose. Black symbols represent the dose indices from the 3D calculation, whereas red symbols represent the dose indices from the 4D calculation. The treatment plan is based on the 3D calculation.

In Table 4-2, the dose at the center of the GTV, and the mean, minimum, and maximum doses in the GTV for patients 1–3 are indicated, respectively. Here, differences between the dose in the ITV of the treatment plan and the dose in the GTV of each treatment fraction are shown as a percentage. The mean doses in each treatment day for patients 1–3 were within -2.2% to -0.8%, -1.4% to +1.5%, and -0.8% to +1.9%, respectively, compared with the corresponding treatment plans. The minimum doses for patient 1–3 were -0.6% to

-3.6%, -2.3% to 1.0%, and -2.4% to 3.0%, respectively.

Table 4-2: Dose at the GTV center and the mean, minimum, and maximum doses for the GTV of patient 1. The differences between the dose in the ITV of the treatment plan and the dose in the GTV of each treatment fraction by 4D calculation are shown as a percentage.

Patient 1:

Index	GTV center		mean		maximum		minimum	
	dose [cGy]	difference[%]	dose [cGy]	difference[%]	dose [cGy]	difference[%]	dose [cGy]	difference[%
Plan	1308.9		1299.1		1315.8		1271.6	
Day1	1292.9	-1.2	1289.0	-0.8	1307.2	-0.7	1263.4	-0.6
Day2	1280.6	-2.2	1274.7	-1.9	1301.5	-1.1	1226.0	-3.6
Day3	1276.7	-2.5	1271.6	-2.1	1296.2	-1.5	1231.8	-3.1
Day4	1274.2	-2.7	1270.1	-2.2	1294.2	-1.6	1233.7	-3.0

Patient 2:

Index	GTV center		mean		maximum		minimum	
	dose [cGy]	difference[%]	dose [cGy]	difference[%]	dose [cGy]	difference[%]	dose [cGy]	difference[%
Plan	885.0		869.2		903.4		810.9	
Day1	858.1	-3.0	857.4	-1.4	907.8	0.5	792.5	-2.3
Day2	868.0	-1.9	865.9	-0.4	905.3	0.2	808.3	-0.3
Day3	880.8	-0.5	877.1	0.9	919.0	1.7	819.3	1.0
Day4	871.8	-1.5	866.7	-0.3	909.9	0.7	805.2	-0.7
Day5	886.5	0.2	882.2	1.5	919.6	1.8	814.0	0.4
Day6	883.2	-0.2	878.6	1.1	915.5	1.3	819.0	1.0
Day7	882.4	-0.3	878.3	1.0	915.6	1.4	818.9	1.0

Patient 3:

Index	GTV center		mean		maximum		minimum	
	dose [cGy]	difference[%]	dose [cGy]	difference[%]	dose [cGy]	difference[%]	dose [cGy]	difference[%
Plan	1186.6		1175.4		1246.4		1068.5	
Day1	1185.1	-0.1	1166.1	-0.8	1228.9	-1.4	1042.6	-2.4
Day2	1200.9	1.2	1183.8	0.7	1235.3	-0.9	1064.9	-0.3
Day3	1211.7	2.1	1188.8	1.1	1239.2	-0.6	1100.0	3.0
Day4	1227.9	3.5	1197.6	1.9	1247.5	0.1	1066.6	-0.2

Finally, in Table 4-3, I summarized the GTV dose by 4D dose calculation compared with the ITV dose by 3D calculation, as described in the previous subsection. The agreement between the mean and maximum doses was very good. However, I observed that a difference of more than 3% was observed in the second day for patient 1, and in the first and fourth days for patient 3.

Table 4-3: Comparison between 3D and 4D dose calculation for 3 lung cancer patients. The doses in the GTV of the 4D calculation are compared with those in the ITV of the 3D calculation.

Patient 1:

Day	mean			maximum			minimum		
	D_{mean3D}(ITV)	D_{mean4D}(GTV)	difference[%]	D_{max3D}(ITV)	D_{max4D}(GTV)	difference[%]	D_{min3D}(ITV)	D_{min4D}(GTV)	difference[%]
1	1282.9	1289.0	0.5	1301.9	1307.2	0.4	1255.5	1263.4	0.6
2	1274.4	1274.7	0.0	1308.4	1301.5	-0.5	1181.2	1226.0	3.8
3	1271.3	1271.6	0.0	1297.7	1296.2	-0.1	1232.8	1231.8	-0.1
4	1267.4	1270.1	0.2	1295.0	1294.2	-0.1	1212.1	1233.7	1.8

Patient 2:

Day	mean			maximum			minimum		
	D_{mean3D}(ITV)	D_{mean4D}(GTV)	difference[%]	D_{max3D}(ITV)	D_{max4D}(GTV)	difference[%]	D_{min3D}(ITV)	D_{min4D}(GTV)	difference[%]
1	859.2	857.4	-0.2	907.7	907.8	0.0	800.1	792.5	-0.9
2	866.2	865.9	0.0	904.1	905.3	0.1	811.7	808.3	-0.4
3	877.1	877.1	0.0	918.4	919.0	0.1	819.4	819.3	0.0
4	868.1	866.7	-0.2	910.1	909.9	0.0	808.5	805.2	-0.4
5	882.2	882.2	0.0	920.0	919.6	0.0	820.3	814.0	-0.8
6	879.2	878.6	-0.1	915.0	915.5	0.1	823.3	819.0	-0.5
7	878.1	878.3	0.0	915.4	915.6	0.0	824.6	818.9	-0.7

Patient 3:

Day	mean			maximum			minimum		
	D_{mean3D}(ITV)	D_{mean4D}(GTV)	difference[%]	D_{max3D}(ITV)	D_{max4D}(GTV)	difference[%]	D_{min3D}(ITV)	D_{min4D}(GTV)	difference[%]
1	1159.0	1166.1	0.6	1235.1	1228.9	-0.5	984.8	1042.6	5.9
2	1178.4	1183.8	0.5	1235.4	1235.3	0.0	1039.4	1064.9	2.4
3	1180.9	1180.8	0.0	1240.7	1239.2	-0.1	1086.9	1081.3	-0.5
4	1184.4	1197.6	1.1	1245.7	1247.5	0.1	1012.1	1066.6	5.4

4.4 Discussion

Dosimetric verification is nowadays considered to be important. In particular, *in vivo* dosimetry during VMAT delivery for a moving target is one of the most challenging current topics in radiation therapy. In this chapter, I have shown a 4D dose calculation system for SBRT-VMAT delivery for lung cancer patients. This work only used the measurement data, that is the kV projection and LINAC log data, both of which were acquired during treatment. The present system can contribute to the quality control and quality assurance of high-precision radiation therapy by detecting a major error in the accuracy of the beam

delivery, treatment planning, patient setup, intra-fractional organ motion, etc.

In a moving phantom experiment, the large discrepancy from the measurement using an ion chamber was found in the 3D calculation. On the other hand, the result of 4D dose calculation agreed well. From comparison between 4-phase and 10-phase 4D CTs, it was found that even 4-phase 4D CBCT performed well in the detection of the interplay effect.

In this experiment, no constraint was applied to the maximum MLC travel speed for the employed VMAT test planning. Since MLC motion behavior could be critical for the dose to a moving target, it was expected that the interplay effect was small for the clinical treatment plan with a maximum MLC travel speed of 0.1 cm/degree. As seen in Table 4-3, the difference between 3D and 4D calculations for the mean and maximum doses was fairly small. However, for the minimum dose, a difference of more than 3% was observed on the second day for patient 1 and on the first and fourth days for patient 3. The tumor motion amplitudes for patients 1 and 3 were considerably larger than that for patient 2 (see Table 3-1). Therefore, even if a constraint on MLC motion was imposed, the effect induced by tumor motion would remain if the motion was considerable. Such an error introduced by periodic motion could be averaged out over the course of fractions, but this is not the case for a few-fraction treatment course of SBRT. Thus, monitoring the individual dose distribution in each phase as well as in each fraction is important with regard to QA for lung SBRT treatment.

The dose distribution reconstructed by in-treatment 4D CBCT and log data may be inconsistent with that of the treatment plan based on the 3D calculation. Even if the 3D dose distribution was comparable, as seen in Section 4.3.2 a), some factors may contribute to a difference from the treatment planning CT scan. These factors include the image quality of CBCT, imperfect machine control, and the geometric sizes, shapes, and locations of the targets, organs, and geometric topography of the patient. As shown in Section 3.3, an approximately 1% difference for the mean dose can be caused by the ROI mapping method for dose calculation on CBCT. For imperfect machine control, the previous study showed that the region yielding 1% difference from the prescription dose was only 0.1% for a lung cancer patient, with the MLC constraint. Unlike the above 2 factors, it is difficult to indicate separately the magnitude of the error caused by the geometrical change of the body and the target. Subtracting the difference arising from the use of CBCT and log data, one may regard the residual error as that arising from its geometrical change. As seen in Table 4-1, where the treatment plan was compared with the 3D calculation by use of CBCT and log data, almost all mean doses in the ITV were within 2%. Hence, the residual error seems to be small. However, the minimum doses in the ITV had a considerable difference. This result implies that the calculation using in-treatment CBCT is essential in order to take into account geometrical changes of the body and the target.

The large deviation from the treatment plan in 4D dose calculation was found on the second, third, and fourth days for patient 1 (Table 4-2). To see this cause in more detail, some beam's eye view (BEV) images on the second day are indicated in Fig. 4-9. A few segments (about 10% of the treatment) blocked a portion of the GTV by MLC leaves. The distance between the GTV (yellow lines) on the end-expiration phase and the upper jaw (Y2) was almost 0.5 cm. On the other hand, this distance on the first day was much larger than that on second day (see the BEVs indicated in Fig. 4-10). The tumor trajectories of this patient were also evaluated, as shown in Fig. 4-11. Only a slight difference of the distributions on the first treatment day from the treatment plan was observed, whereas a visible difference on the other days was observed. The decrease of the dose in the upper lesion of the GTV during the second, third, and fourth fractions seemed to be caused by the unexpected location of the target.

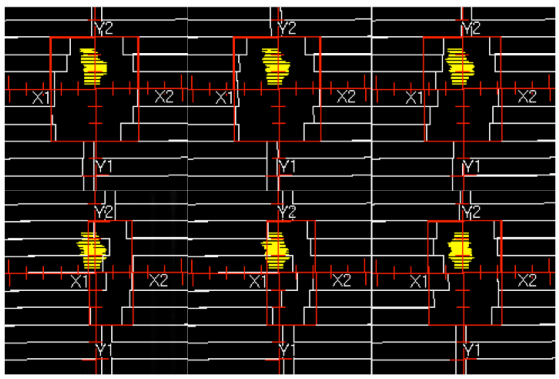

Fig. 4-9: Example of beam's eye view on the second day for patient 1. The yellow lines denote the GTV from in-treatment 4D CBCT. The distance between the GTV on the end-expiration phase and the upper jaw (Y2) was almost 0.5 cm.

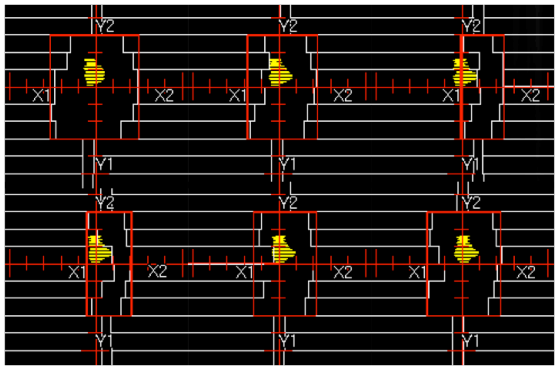

Fig. 4-10: Example of beam's eye view on first day for patient 1. The distance between the GTV on the end-expiration phase and the upper jaw (Y2) was almost 1.0 cm.

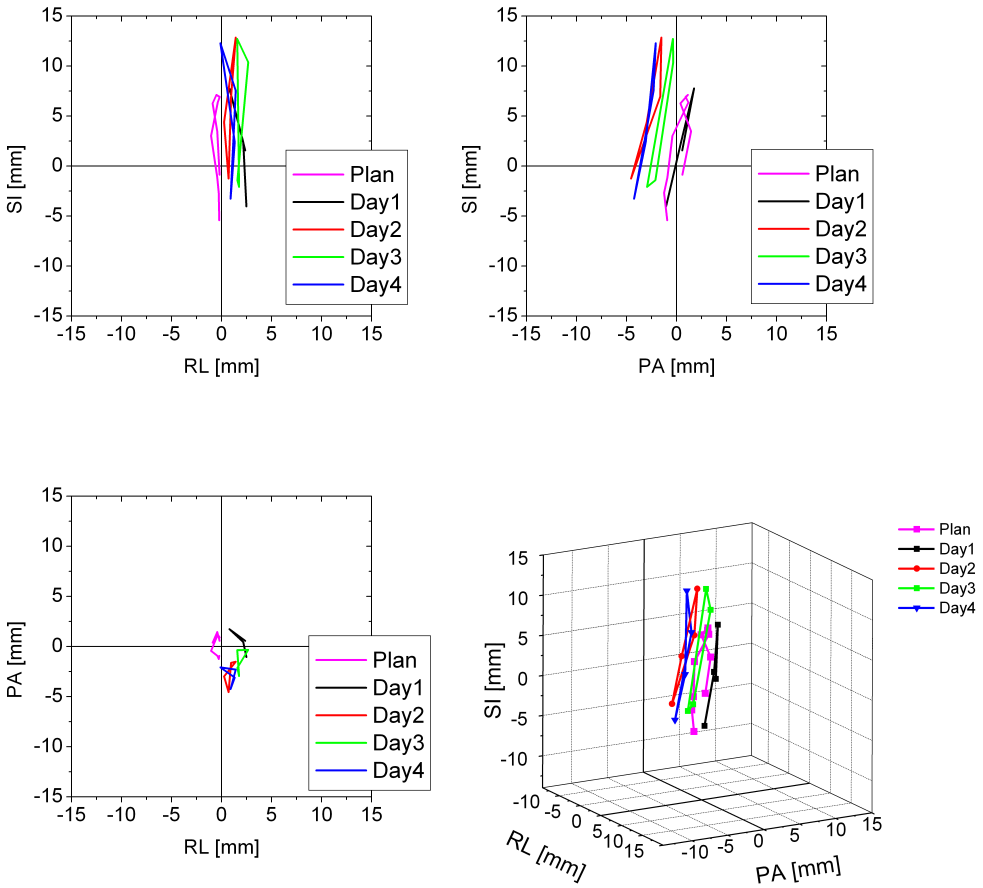

Fig. 4-11: Tumor trajectory of the center of the GTV for patient 1. SI, PA, and RL indicate superior-inferior, anterior-posterior, and right-left direction, respectively.

5 Summary

I developed a verification method for moving targets using 4D dose calculation based on the information acquired during treatment. The beam shape, direction, and intensity were constructed from the LINAC log data, which was in excellent agreement with the EPID measurement for the MLC location. With those data, the dose calculation was performed on each phase of in-treatment 4D CBCT by means of the ROI mapping method. The predicted dose value of the center of the target in a moving phantom agreed well with the measurement dose.

Actual dose distributions for 3 lung cancer patients with this technique were evaluated and compared with those of the treatment plan. A small but significant dose difference between the 3D and 4D calculations was observed for the case of large target traveling. Also, a day-to-day fluctuation of the delivered dose was observed for all patients. Although the VMAT plan with MLC speed constraint was effective in reducing the interplay effect, the difference from the plan should not be negligible.

Patient setup and correction of the patient position were extremely important for the reproducibility of the treatment plan for high-precision radiotherapy. The dose error could be enhanced drastically if the target trajectory deviated from the planned ITV. If the actual dose

was under- or overestimated, the treatment plan for the next fraction could be modified for making the cumulative dose up to that fraction. 4D ART can be potentially developed based on the present method.

The 4D dose calculation described in this thesis is the first method to use only data acquired during actual delivery. Still, there is a room for improvement to the present 4D dose calculation method. I employed the ROI mapping method, which fits the individual anatomical information without any artifact on 4D CBCT. However, the application of the ROI mapping method to a lung cancer case may generate an error in the dose at the boundary of target, since one density averaged in the GTV was assigned. In addition, interobserver variation has to be considered because almost all structures were drawn by hand. For clinical application, calculation time is another problem; it takes almost 6 hours for 1 fraction, including the time needed for drawing the structures as well as the dose calculation time. An improvement in quality of 4D CBCT images, possibly by auto segmentation of the ROIs, is also needed.

Acknowledgements

Throughout this work, I got to know many people whom I am very grateful for their help and encouragement. I would like to express my deep appreciation to all of them. I would like to express my sincere gratitude to my supervisor, Dr. Keiichi Nakagawa for his guidance and encouragement during my thesis work. I am especially for appropriate advices. I am indebted to Dr. Akihiro Haga, the leader of the medical physics group, for his constant support, encouragement and help that make my research of great achievement and my study life unforgettable. I also obliged to Dr. Yoshitaka Masutani, Dr. Hideomi Yamashita, Dr. Akira Sakumi, Dr. Toshikazu Imae, and Mr. Satoshi Kida for helpful discussions and a lot of advices. In addition, I would like to thank the other members of the Department of Radiation Oncology, The University of Tokyo hospital for warm support and continuous encouragement. I would like to express thanks to Prof. Atsuro Terahara and all the members of the Department of Radiation Oncology, Toho University Omori hospital for valuable advices and encouragement. Thanks also go to Dr. Di Yan, Dr. Jian Liang, Dr. An Qin, and Dr. Ling Zhuang for useful advice and help during my stay in U.S.A. I am thankful to Dr. Kiyoshi Yoda and Dr. Yoshio Iwai, Elekta inc. for valuable discussions and technical support.

The author finally expressed special thanks to his family and friends for helps and support.

Reference

[1]: [http://www.mhlw.go.jp/toukei/saikin/hw/jinkou/geppo/nengai11/kekka03.html].

[2]: [http://ganjoho.ncc.go.jp/professional/statistics/statistics.html]

[3]: ICRU Report 50. Prescribing, Recording, and Reporting Photon Beam Therapy, International Commission on Radiation Units and Measurements, Bethesda, MD (1993).

[4]: ICRU Report 62. Prescribing, Recording, and Reporting Photon Beam Therapy (Supplement to ICRU Report 50), International Commission on Radiation Units and Measurements, Bethesda, MD (1999).

[5]: ICRU Report 83. Prescribing, Recording, and Reporting photon-beam intensity-modulated radiation therapy (IMRT), International Commission on Radiation Units and Measurements, Bethesda, MD (2010).

[6]: Bortfeld T., Kahler D., Waldron T., Boyer A., "X-ray field compensation with multileaf collimators", *International Journal of Radiation Oncology Biology Physics* 28 (1994): 723-730.

[7]: Siochi R., "Minimizing static intensity modulation delivery time using an intensity solid paradigm", *International Journal of Radiation Oncology Biology Physics* 43 (1999): 671-680.

[8]: Convery D. J., Rosenbloom M. E., "The generation of intensity-modulated fields for conformal radiotherapy by dynamic collimation", *Physics in Medicine and Biology* 37 (1992): 1359-1374.

[9]: Dirkx M., Heijmen B., van Santvoort J., "Leaf trajectory calculation for dynamic multileaf collimation to realize optimized fluence profiles", *Physics in Medicine and Biology* 43 (1998): 1171-1184.

[10]: Ling C., Burman C., Chui C., Kutcher G., Leibel S., LoSasso T., Mohan R., Bortfeld T., Reinstein L., Spirou S., Wang X., Wu Q., Zelefsky M., Fuks Z., "Conformal radiation treatment of prostate cancer using inversely-planned intensity-modulated photon beams produced with dynamic multileaf collimation", *International Journal of Radiation Oncology Biology Physics* 35 (1996): 721-730.

[11]: Spirou S. V., Chen C. S., "Generation of arbitrary intensity profiles by dynamic jaws or

multileaf collimators", *Medical Physics* 23 (1996): 1-8.

[12]: Donovan E, Bleackley N, Evans P, Reise S, Yarnold J. "Dose-position and dose-volume histogram analysis of standard wedged and intensity modulated treatments in breast radiotherapy", *British Journal of Radiology* 75 (2002): 967-973.

[13]: Donovan E, Bleakley N, Denholm E, Evans P, Gothard L, Hanson J, Peckitt C, Reise S, Ross G, Sharp G, Symonds-Tayler R, Tait D, Yarnold J. "Randomised trial of standard 2D radiotherapy (RT) versus intensity modulated radiotherapy (IMRT) in patients prescribed breast radiotherapy", *Radiotherapy and Oncology* 82 (2007): 254-264.

[14]: Jabbari S, Kim H, Feng M, Lin A, Tsien C, Elshaikh M, Terrel J, Murdoch-Kinch C, Eisbruch A. "Matched case–control study of quality of life and xerostomia after intensity-modulated radiotherapy or standard radiotherapy for head-and-neck cancer: initial report", *International Journal of Radiation Oncology Biology Physics* 63 (2005): 725-731.

[15]: Yu C. X., "Intensity-modulated arc therapy with dynamic multileaf collimation: an alternative to tomotherapy", *Physics in Medicine and Biology* 40 (1995): 1435-1449.

[16]: Otto K. "Volumetric modulated arc therapy: IMRT in a single gantry arc", Medical Physics 35 (2008): 310-317.

[17]: Bedford L., Alan W., "Commissioning of volumetric modulated arc therapy (VMAT)", *International Journal of Radiation Oncology Biology Physics* 73 (2009): 537-545.

[18]: Korreman S., Medin J., Kjaer-Kristoffersen F., "Dosimetric verification of RapidArc treatment delivery", *Acta Oncologica* 48 (2009): 185-191.

[19]: Schreibmann E., Dhabaan A., Elder E., Fox T., "Patient-specific quality assurance method for VMAT treatment delivery", *Medical Physics* 36 (2009): 4530-4535.

[20]: Leksell L., "The stereotaxic method and radiosurgery of the brain", *Acta Chirurgica Scandinavica* 102 (1951): 316-319.

[21]: Leksell L., "Trigeminal neuralgia. Some neurophysiologic aspects and a new method of therapy", *Läkartidningen* 68 (1971): 5145-5148.

[22]: Blomgren H., Lax I., Näslund I., Svanström R., "Stereotactic high dose fraction radiation therapy of extracranial tumors using an accelerator: clinical experience of the first thirty-one patients", *Acta Oncologica* 34 (1995): 861-870.

[23]: Jaffray D., Siewerdsen J., Wong J., "Flat-panel cone-beam computed tomography for image-guided radiation therapy", *International Journal of Radiation Oncology Biology Physics* 53 (2002): 1337-1349.

[24]: Jaffray D., Drake D., Moreau M., Martinez A., Wong J., "A radiographic and tomographic imaging system integrated into a medical linear accelerator for localization of bone and soft-tissue targets", *International Journal of Radiation Oncology Biology Physics* 45 (1999): 773-789.

[25]: Jaffray D., Siewerdsen J., "Cone-beam computed tomography with a flat-panel imager: initial performance characterization", *Medical Physics* 27 (2000): 1311-1323.

[26]: Jaffray C., Yang J., Norman J., Elastase Mimics "Pancreatitis-Induced Hepatic Injury via Inflammatory Mediators", *Journal of Surgical Research*, 90 (2000): 95–101.

[27]: Sonke J., Rossi M., Wolthaus J., van Herk M., Damen E., Belderbos J., "Frameless stereotactic body radiotherapy for lung cancer using four-dimensional cone beam CT guidance", *International Journal of Radiation Oncology Biology Physics* 74.2 (2009): 567-574.

[28]: Sonke J., Zijp L., Remeijer P., van M., "Respiratory correlated cone beam CT", *Medical Physics* 32 (2005): 1176-86.

[29]: Nakagawa K., Yamashita H., Shiraishi K., Igaki H., Terahara A., Nakamura N., Ohtomo K., Saegusa S., Shiraki T., Oritate T., Yoda K., "Verification of in-treatment tumor position using kilovoltage cone-beam computed tomography: A preliminary study", *International Journal of Radiation Oncology Biology Physics* 69 (2007): 970-973.

[30]: Li T., Thongphiew D., Zhu X., Lee W., Vujaskovic Z., Yin F., Wu Q., "Adaptive prostate IGRT combining online re-optimization and re-positioning: a feasibility study", *Physics in Medicine and Biology* 56 (2011) 1243–1258.

[31]: Court L., Dong L., Lee A., Cheung R., Bonnen M., O'Daniel J., Wang H., Mohan R., Kuban D., "An automatic CT-guided adaptive radiation therapy technique by online modification of multileaf collimator leaf positions for prostate cancer", *International Journal of Radiation Oncology Biology Physics* 62 (2005): 154-163.

[32]: Yan D., Lockman D., Martinez A., Wong J., Brabbins D., Vicini F., Liang J., Kestin L., "Computed tomography guided management of interfractional patient variation", *Seminars in Radiation Oncology* 15 (2005): 168-179.

[33]: Yan D., Ziaja E., Jaffray D., Wong J., Brabbins D., Vicini F., Martinez A., "The use of adaptive radiation therapy to reduce setup error: a prospective clinical study", *International Journal of Radiation Oncology Biology Physics* 41 (1998): 715-720.

[34]: Yan D., Lockman D., Brabbins D., Tyburski L., Martinez A., "An off-line strategy for constructing a patient-specific planning target volume in adaptive treatment process for prostate cancer", *International Journal of Radiation Oncology Biology Physics* 48 (2000): 289-302.

[35]: Yan D., Liang J., "Expected treatment dose construction and adaptive inverse planning optimization: Implementation for offline head and neck cancer adaptive radiotherapy", *Medical Physics* 40 (2013): 021719.

[36]: Bzdusek K., Friberger H., Eriksson K., Hårdemark B., Robinson D., Kaus M., "Development and evaluation of an efficient approach to volumetric arc therapy planning", *Medical Physics* 36 (2009): 2328-2339.

[37]: Higgins P., Alaei P., Gerbi B., Dusenbery K., "In vivo diode dosimetry for routine quality assurance in IMRT", *Medical Physics* 30 (2003): 3118-3123.

[38]: McNutt T., Mackie T., Reckwerdt P., Paliwal B., "Modeling dose distributions from portal dose images using the convolution/superposition method", *Medical Physics* 23 (1996): 1381-1392.

[39]: Kapatoes JM., Olivera GH., Balog JP., Keller H., Reckwerdt PJ., Mackie TR., "On the accuracy and effectiveness of dose reconstruction for tomotherapy", *Physics in Medicine and Biology* 46 (2001): 943.

[40]: Biancia C., Yorke E., Chui C., Giraud P., "Comparison of end normal inspiration and expiration for gated intensity modulated radiation therapy (IMRT) of lung cancer", *Radiotherapy and Oncology* 75 (2005): 149-156.

[41]: Stevens C., Munden R., Forster K., Kelly J., Liao Z., Starkschall G., Tucker S., Komaki R., "Respiratory-driven lung tumor motion is independent of tumor size, tumor location, and pulmonary function", *International Journal of Radiation Oncology Biology Physics* 51 (2001): 62-68.

[42]: Seppenwoolde Y., Shirato H., Kitamura K., Shimizu S., van Herk M., Lebesque J., Miyasaka K., "Precise and real-time measurement of 3D tumor motion in lung due to breathing and heartbeat, measured during radiotherapy", *International Journal of Radiation*

Oncology Biology Physics 53 (2002): 822-834.

[43]: Hoisak D. P., Sixel K. E., Tirona R., Cheung P., Pignol P., "Correlation of lung tumor motion with external surrogate indicators of respiration", *International Journal of Radiation Oncology Biology Physics* 60 (2004): 1298-1306.

[44]: Tsunashima Y., Sakae T., Shioyama Y., Kagei K., Terunuma T., Nohtomi A., Akine Y., "Correlation between the respiratory waveform measured using a respiratory sensor and 3D tumor motion in gated radiotherapy", *International Journal of Radiation Oncology Biology Physics* 60 (2004): 951-958.

[45]: Koch N., Liu H., Starkschall G., Jacobson M., Forster K., Liao Z., Komaki R., Stevens C., "Evaluation of internal lung motion for respiratory-gated radiotherapy using MRI: Part I—Correlating internal lung motion with skin fiducial motion", *International Journal of Radiation Oncology Biology Physics* 60 (2004): 1459-1472.

[47]: Nakagawa K., Kida S., Haga A., Masutani Y., Yamashita H., Imae T., Tanaka K., Ohtomo K., Iwai Y., Yoda K., "Cone beam computed tomography data acquisition during VMAT delivery with subsequent respiratory phase sorting based on projection image cross-correlation", *Journal of Radiation Research* 52 (2011): 112-113.

[48]: Balter J., Ten Haken R., Lawrence T., Lam K., Robertson J., "Uncertainties in CT-based radiation therapy treatment planning associated with patient breathing", *International Journal of Radiation Oncology Biology Physics* 36 (1996): 167-174.

[49]: Chen G., Kung J., Beaudette K., "Artifacts in computed tomography scanning of moving objects", *Seminars in Radiation Oncology* 14 (2004): 19-26.

[50]: Mechalakos J., Yorke E., Mageras G., Hertanto A., Jackson A., Obcemea C., Rosenzweig K., Clifton Ling C., "Dosimetric effect of respiratory motion in external beam radiotherapy of the lung", *Radiotherapy and Oncology* 71 (2004): 191-200.

[51]: Van Herk M. "Is it safe to ignore respiration during external beam radiotherapy?", In *The 14 th International Conference on the use of Computers in Radiotherapy*. Jeong Publishing, Seoul, South Korea, (2004): 44.

[52]: Ford E., Mageras G., Yorke E., Rosenzweig K., Wagman R., Ling C., "Evaluation of respiratory movement during gated radiotherapy using film and electronic portal imaging", *International Journal of Radiation Oncology Biology Physics* 52 (2002): 522-531.

[53]: Yorke E., Rosenzweig K., Wagman R., Mageras G., "Inter-fractional anatomic variation in patients treated with respiration-gated radiotherapy", *Journal of Applied Clinical Medical Physics* 6 (2005): 12-32.

[54]: van Herk M., Remeijer P., Rasch C., Lebesque J., "The probability of correct target dosage: dose-population histograms for deriving treatment margins in radiotherapy", *International Journal of Radiation Oncology Biology Physics* 47 (2000): 1121-1135.

[55]: Ohara K., Okumura T., Akisada M., Inada T., Mori T., Yokota H., Calaguas M., "Irradiation synchronized with respiration gate", *International Journal of Radiation Oncology Biology Physics* 17 (1989): 853-857.

[56]: Tada T., Minakuchi K., Fujioka T., Sakurai M., Koda M., Kawase I., Nakajima T., Nishioka M., Tonai T., Kozuka T., "Lung cancer: intermittent irradiation synchronized with respiratory motion--results of a pilot study", *Radiology* 207 (1998): 779-783.

[57]: Shirato H., Shimizu S., Kitamura K., Nishioka T., Kagei K., Hashimoto S., Aoyama H., Kunieda T., Shinohara N., Dosaka-Akita H., Miyasaka K., "Four-dimensional treatment planning and fluoroscopic real-time tumor tracking radiotherapy for moving tumor", *International Journal of Radiation Oncology Biology Physics* 48 (2000): 435-442.

[58]: Shirato H., Shimizu S., Kunieda T., Kitamura K., van Herk M., Kagei K., Nishioka T., Hashimoto S., Fujita K., Aoyama H., Tsuchiya K., Kudo K., Miyasaka K., "Physical aspects of a real-time tumor-tracking system for gated radiotherapy", *International Journal of Radiation Oncology Biology Physics* 48 (2000): 1187-1195.

[59]: Kubo H., Len P., Minohara S., Mostafavi H., "Breathing-synchronized radiotherapy program at the University of California Davis Cancer Center", *Medical Physics* 27 (2000): 346-353.

[60]: Blomgren H., Lax I., Näslund I., Svanström R., "Stereotactic high dose fraction radiation therapy of extracranial tumors using an accelerator: clinical experience of the first thirty-one patients", *Acta Oncologica* 34 (1995): 861-870.

[61]: Wong J., Sharpe M., Jaffray D., Kini V., Robertson J., Stromberg J., Martinez A., "The use of active breathing control (ABC) to reduce margin for breathing motion", *International Journal of Radiation Oncology Biology Physics* 44 (1999): 911-919.

[62]: Mah D., Hanley J., Rosenzweig K., Yorke E., Braban L., Ling C., Leibel S., Mageras G., "Technical aspects of the deep inspiration breath-hold technique in the treatment of thoracic

cancer", *International Journal of Radiation Oncology Biology Physics* 48 (2000): 1175-1185.

[63]: Stevens C., Munden R., Forster K., Kelly J., Liao Z., Starkschall G., Tucker S., Komaki R., "Respiratory-driven lung tumor motion is independent of tumor size, tumor location, and pulmonary function", *International Journal of Radiation Oncology Biology Physics* 51 (2001): 62-68.

[64]: Rosenzweig K., Hanley J., Mah D., Mageras G., Hunt M., Toner S., Burman C., Ling C., Mychalczak B., Fuks Z., Leibel S., "The deep inspiration breath-hold technique in the treatment of inoperable non–small-cell lung cancer", *International Journal of Radiation Oncology Biology Physics* 48 (2000): 81-87.

[65]: Ozhasoglu C., Murphy M., "Issues in respiratory motion compensation during external-beam radiotherapy", *International Journal of Radiation Oncology Biology Physics* 52 (2002): 1389-1399.

[66]: Mageras G., Yorke E., Rosenzweig K., Braban L., Keatley E., Ford E., Leibel S., Ling C., "Fluoroscopic evaluation of diaphragmatic motion reduction with a respiratory gated radiotherapy system", *Journal of Applied Clinical Medical Physics* 2 (2001): 191-200.

[67]: Murphy M., "Tracking moving organs in real time", *Seminars in Radiation Oncology* 14, (2004): 91-100.

[68]: Seiler P., Blattmann H., Kirsch S., Muench R., Schilling C., "A novel tracking technique for the continuous precise measurement of tumour positions in conformal radiotherapy", *Physics in Medicine and Biology* 45 (2000): N103.

[69]: Russell K., Skrumeda L., Gisselberg M., Hadford E., Humphries D., Sandler H., Roach M., Kupelian P., Mate T., "Biocompatibility of a wireless electromagnetic transponder permanent implant for accurate localization and continuous tracking of tumor targets", *International Journal of Radiation Oncology Biology Physics* 57 (2003): S396-S397.

[70]: Meeks S. L., Buatti J. M., Bouchet L. G., Bova F. J., Ryken T. C., Pennington E. C., Anderson K. M., Friedman W. A., "Ultrasound-guided extracranial radiosurgery: technique and application", *International Journal of Radiation Oncology Biology Physics* 55 (2003): 1092-1101.

[71]: Yu C., Jaffray D., Wong J., "The effects of intra-fraction organ motion on the delivery of dynamic intensity modulation", *Physics in Medicine and Biology* 43 (1998): 91-104.

[72]: Kissick M., Boswell S., Jeraj R., Mackie T., "Confirmation, refinement, and extension of a study in intrafraction motion interplay with sliding jaw motion", *Medical Physics* 32 (2005): 2346-2350.

[73]: Bortfeld T., Jokivarsi K., Goitein M., Kung J., Jiang S., "Effects of intra-fraction motion on IMRT dose delivery: statistical analysis and simulation", *Physics in Medicine and Biology* 47 (2002): 2203-2220.

[74]: Kubo H., Wang L., "Compatibility of Varian 2100C gated operations with enhanced dynamic wedge and IMRT dose delivery", *Medical Physics* 27 (2000): 1732-1738.

[75]: Keall P., Kini V., Vedam S., Mohan R., "Motion adaptive x-ray therapy: a feasibility study", *Physics in Medicine and Biology* 46 (2001): 1-10.

[76]: Yu C., Jaffray D., Wong J., "The effects of intra-fraction organ motion on the delivery of dynamic intensity modulation", *Physics in Medicine and Biology* 43 (1998): 91-104

[77]: Bortfeld T., Jokivarsi K., Goitein M., Kung J., Jiang S., "Effects of intra-fraction motion on IMRT dose delivery: statistical analysis and simulation", *Physics in Medicine and Biology* 47 (2002): 2203-2220.

[78]: George R., Keall P., Kini V., Vedam S., Siebers J., Wu Q., Lauterbach M., Arthur D., Mohan R., "Quantifying the effect of intrafraction motion during breast IMRT planning and dose delivery", *Medical Physics* 30 (2003): 552-62.

[79]: Chui C. S., Yorke E., Hong L., "The effects of intra-fraction organ motion on the delivery of intensity-modulated field with a multileaf collimator", *Medical Physics* 30 (2003): 1736-1746.

[80]: Jiang S., Pope C., Al K., Kung J., Bortfeld T., Chen G., "An experimental investigation on intra-fractional organ motion effects in lung IMRT treatments", *Physics in Medicine and Biology* 48 (2003): 1773-1784.

[81]: Bortfeld T., Jokivarsi K., Goitein M., Kung J., Jiang S., "Effects of intra-fraction motion on IMRT dose delivery: statistical analysis and simulation", *Physics in Medicine and Biology* 47 (2002): 2203-2220.

[82]: Seppenwoolde Y., Shirato H., Kitamura K., Shimizu S., van Herk M., Lebesque J., Miyasaka K., "Precise and real-time measurement of 3D tumor motion in lung due to breathing and heartbeat, measured during radiotherapy", *International Journal of Radiation*

Oncology Biology Physics 53 (2002): 822-834.

[83]: Ozhasoglu C., Murphy M. "Issues in respiratory motion compensation during external-beam radiotherapy", *International Journal of Radiation Oncology Biology Physics* 52 (2002): 1389-1399.

[84]: Nakagawa K., Aoki Y., Akanuma A., Onogi Y., Terahara A., Sakata K., Muta N., Sasaki Y., Kawakam H., Hanakawa K., "Real-time beam monitoring in dynamic conformation therapy", *International Journal of Radiation Oncology Biology Physics* 30 (1994): 1233–1238.

[85]: Kida S., Masutani Y., Yamashita H., Imae T., Matsuura T., Saotome N., Ohtomo K., Nakagawa K., Haga A., "In-treatment 4D cone-beam CT with image-based respiratory phase recognition", *Radiological Physics and Technology* 5 (2012): 138–147.

[86]: McDermott L., Nijsten S., Sonke J., Partridge M., van Herk M., Mijnheer B., "Comparison of ghosting effects for three commercial a-Si EPIDs", *Medical Physics* 33 (2006): 2448-2451.

[87]: Budgell G., Mott J., Williams P., Brown K., "Requirements for leaf position accuracy for dynamic multileaf collimation", *Physics in Medicine and Biology* 45 (2000): 1211-1227.

[88]: Burman C., Chui C., Kutcher G., Leibel S., Zelefsky M., LoSasso T., Spirou S., Wu Q., Yang J., Stein J., Mohan R., Fuks Z., Ling C., "Planning, delivery, and quality assurance of intensity-modulated radiotherapy using dynamic multileaf collimator: a strategy for large-scale implementation for the treatment of carcinoma of the prostate", *International Journal of Radiation Oncology Biology Physics* 39 (1997): 863-873.

[89]: LoSasso T., Chui C., Ling C., "Comprehensive quality assurance for the delivery of intensity modulated radiotherapy with a multileaf collimator used in the dynamic mode", *Medical Physics* 28 (2001): 2209-2219.

[90]: Ling C., Zhang P., Archambault Y., Bocanek J., Tang G., Losasso T., "Commissioning and quality assurance of RapidArc radiotherapy delivery system", *International Journal of Radiation Oncology Biology Physics* 72 (2008): 575-581.

[91]: Oliver M., Gagne I., Bush K., Zavgorodni S., Ansbacher W., Beckham W., "Clinical significance of multi-leaf collimator positional errors for volumetric modulated arc therapy", *Radiotherapy and Oncology* 97 (2010): 554-560.

[92]: Tatsumi D., Hosono N., Nakada R., Ishii K., Tsutsumi S., Inoue M., Ichida T., Miki Y., "Direct impact analysis of multi-leaf collimator leaf position errors on dose distributions in volumetric modulated arc therapy: a pass rate calculation between measured planar doses with and without the position errors", *Physics in Medicine and Biology* 56 (2011): N237.

[93]: Betzel G., Yi B., Niu Y., Yu C., "Is RapidArc more susceptible to delivery uncertainties than dynamic IMRT?", *Medical Physics* 39 (2012) : 5882–5890.

[94]: Qian J., Lee L., Liu W., Chu K., Mok E., Luxton G., Le T., Xing L., "Dose reconstruction for volumetric modulated arc therapy (VMAT) using cone-beam CT and dynamic log files", *Physics in Medicine and Biology* 55 (2010) : 3597–3610.

[95]: Haga A., Sakumi A., Okano Y., Itoh S., Saotome N., Kida S., Igaki H., Shiraishi K., Yamashita H., Ohtomo K., Nakagawa K., "Dose verification of volumetric modulated arc therapy (VMAT) by use of in-treatment linac parameters", *Radiological Physics and Technology* 6 (2013): 335–342.

[96]: Bakhtiari M., Kumaraswamy L., Bailey D., de Boer S., Malhotra H., Podgorsak M., "Using an EPID for patient-specific VMAT quality assurance", *Medical Physics* 38 (2011): 1366–73.

[97]: Bijhold J., Gilhuijs K., van Herk M., Meertens H., "Radiation field edge detection in portal images", *Physics in Medicine and Biology* 36 (1991): 1705–1710.

[98]: Canny J., "A computational approach to edge detection", Pattern Analysis and Machine Intelligence, *IEEE Transactions* 6 (1986): 679-698.

[99]: Nakagawa K., Haga A., Shiraishi K., Yamashita H., Igaki H., Terahara A., Ohtomo K., Saegusa S., Shiraki T., Oritate T., Yoda K., "First clinical cone-beam CT imaging during volumetric modulated arc therapy", Radiotherapy and Oncology : *Journal of the European Society for Therapeutic Radiology and Oncology* 90 (2009): 422–423.

[100]: Nakagawa K., Kida S., Haga A., Masutani Y., Yamashita H., Imae T., Tanaka K., Ohtomo K., Iwai Y., Yoda K., "Cone Beam Computed Tomography Data Acquisition during VMAT Delivery with Subsequent Respiratory Phase Sorting Based on Projection Image Cross-correlation", *Journal of Radiation Research* 52 (2011): 112-113.

[101]: Yoo S., Yin F. "Dosimetric feasibility of cone-beam CT-based treatment planning compared to CT-based treatment planning", *International Journal of Radiation Oncology Biology Physics* 66 (2006): 1553-1561.

[102]: Siewerdsen H., Jaffray D., "Cone-beam computed tomography with a flat-panel imager: magnitude and effects of x-ray scatter", *Medical Physics* 28 (2001): 220-231.

[103]: Thomas S., "Relative electron density calibration of CT scanners for radiotherapy treatment planning", *The British Journal of Radiology* 72 (1999): 781–786.

[104]: Houser C., Nawaz A., Galvin J., Xiao Y., "Quantitative Evaluation of Cone Beam CT Data Used for Treatment Planning" *Medical Physics* 33 (2006): 2285.

[105]: van Zijtveld M., Dirkx M., Heijmen B., "Correction of conebeam CT values using a planning CT for derivation of the “dose of the day”", *Radiotherapy and Oncology* 85 (2007): 195-200.

[106]: Richter A., Hu Q., Steglich D., Baier K., Wilbert J., Guckenberger M., Flentje M., "Investigation of the usability of conebeam CT data sets for dose calculation", *Radiation Oncology* 3 (2008): 42.

[107]: Hu W., Ye J., Wang J., Ma X., Zhang Z., "Use of kilovoltage X-ray volume imaging in patient dose calculation for head-and-neck and partial brain radiation therapy", *Radiation Oncology* 5 (2010): 29.

[108]: Yang Y., Schreibmann E., Li T., Wang C., Xing L., "Evaluation of on-board kV cone beam CT (CBCT)-based dose calculation", *Physics in Medicine and Biology* 52 (2007): 685–705.

[109]: Tucking T., Nill S., Oelfke U. "Dose calculation on linac integrated KV-cone beam CT", *Radiotherapy and Oncology* 81(Supplement 1) (2006): 26.

[110]: Morin O., Chen J., Aubin M., Gillis A., Aubry F., Bose S., Chen H., Descovich M., Xia P., Pouliot J., "Dose calculation using megavoltage cone-beam CT", *International Journal of Radiation Oncology, Biology, Physics* 67 (2007): 1201–10.

[111]: Létourneau D., Wong R., Moseley D., Sharpe M., Ansell S., Gospodarowicz M., Jaffray D., "Online planning and delivery technique for radiotherapy of spinal metastases using cone-beam CT: image quality and system performance", *International Journal of Radiation Oncology, Biology, Physics* 67 (2007): 1229–37.

[112]: Chi Y., Wu Q., Yan D., "Dose Calculation On Cone Beam CT (CBCT)." Medical Physics 34 (2007): 2438.

[113]: Depuydt T., Hrbacek J., Slagmolen P., Van den Heuvel F., "Cone-beam CT Hounsfield

unit correction method and application on images of the pelvic region", *Radiotherapy and Oncology* 81 (2006): S29–S30.

[114]: Houser C., Nawaz A, Galvin J., Xiao Y., "Quantitative Evaluation of Cone Beam CT Data Used for Treatment Planning", *Medical Physics* 33 (2006): 2285.

[115]: Lee L., Le Q., Xing L., "Retrospective IMRT dose reconstruction based on cone-beam CT and MLC log-file", *International Journal of Radiation Oncology Biology Physics* 70 (2008): 634-644.

[116]: Marchant T., Moore C., Rowbottom C., MacKay R., Williams P., "Shading correction algorithm for improvement of cone-beam CT images in radiotherapy", *Physics in Medicine and Biology* 53 (2008): 5719–33.

[117]: Paliwal B., Tewatia D., Orton N., Tome W., Basavatia A., "Cone Beam CT Based Treatment Planning", *Medical Physics* 33 (2006): 2029.

[118]: Convery D., Rosenbloom M. "Treatment delivery accuracy in intensity-modulated conformal radiotherapy", *Physics in Medicine and Biology* 40 (1995): 979-979.

[119]: Jiang S., Pope C., Al K., Kung J., Bortfeld T., Chen G., "An experimental investigation on intra-fractional organ motion effects in lung IMRT treatments", *Physics in Medicine and Biology* 48 (2003): 1773–1784.

[120]: Court L., Wagar M., Ionascu D., Berbeco R., Chin L., Bortfeld T., Jokivarsi K., Goitein M., Kung J., Jiang S., "Effects of intra-fraction motion on IMRT dose delivery: statistical analysis and simulation", *Physics in Medicine and Biology* 47 (2002): 2203–2220.

[122]: Court L., Seco J., Lu Q., Ebe K., Mayo C., Ionascu D., Winey B., Giakoumakis N., Aristophanous M., Berbeco R., Rottman J., Bogdanov M., Schofield D., Lingos T., "Use of a realistic breathing lung phantom to evaluate dose delivery errors", *Medical Physics* 37 (2010): 5850–5857.

[123]: Li H., Li Y., Zhang X., Li X., Liu W., Gillin M., Zhu X., "Dynamically accumulated dose and 4D accumulated dose for moving tumors", *Medical Physics* 39 (2012): 7359–7367.

[124]: Ong C., Verbakel W., Cuijpers J., Slotman B., Senan S., "Dosimetric impact of interplay effect on RapidArc lung stereotactic treatment delivery", *International Journal of Radiation Oncology, Biology, Physics* 79 (2011): 305–311.

[125]: Rao M., Wu J., Cao D., Wong T., Mehta V., Shepard D., Ye J., "Dosimetric impact of

breathing motion in lung stereotactic body radiotherapy treatment using image-modulated radiotherapy and volumetric modulated arc therapy", *International Journal of Radiation Oncology, Biology, Physics* 83 (2012): e251–256.

[126]: Cedric X., David Y., Jaffray A., Wong J., "The effects of intra-fraction organ motion on the delivery of dynamic intensity modulation." *Physics in Medicine and Biology* 43.1 (1998): 91-104.

[127]: Feygelman V., Zhang G., Stevens C., "Initial dosimetric evaluation of SmartArc-a novel VMAT treatment planning module implemented in a multi-vendor delivery chain." *Journal of Applied Clinical Medical Physics* 11 (2010): 99-116.

[128]: Feygelman V., Stambaugh C., Zhang G., Hunt D., Opp D., Wolf T., Nelms B., "Motion as a perturbation: measurement-guided dose estimates to moving patient voxels during modulated arc deliveries", *Medical Physics* 40 (2013): 021708.

[129]: Court L., Wagar M., Berbeco R., Reisner A., Winey B., Schofield D., Ionascu D., Allen A., Popple R., Lingos T., "Evaluation of the interplay effect when using RapidArc to treat targets moving in the craniocaudal or right-left direction", *Medical Physics* 37 (2010): 4–11.

[130]: Kida S., Saotome N., Masutani Y., Yamashita H., Ohtomo K., Nakagawa K., Sakumi A., Haga A., "4D-CBCT reconstruction using MV portal imaging during volumetric modulated arc therapy", *Radiotherapy and Oncology* 100 (2011): 380–385.

A) Appendix: Dose in each phase for 4D calculation

The beam delivery information recorded in the log data was linked with the respiratory signal of the patient in the individual fraction detected by the in-treatment kV imaging. Thus, the MU values recorded in the log data were divided into 4 respiratory phase bins. Figure A-1 shows the results of MU values assigned into 4 respiratory phases for patients 1–3 in Chapter 4.

Patient 1

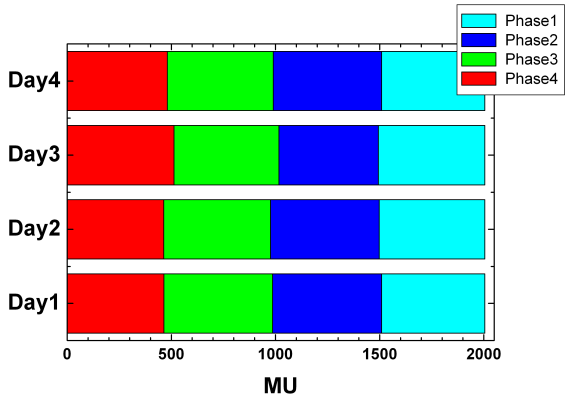

Patient 2

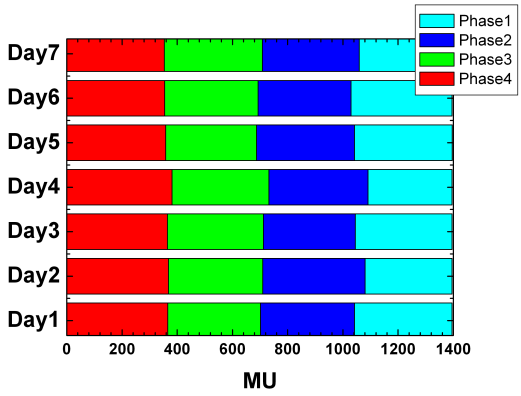

Patient 3

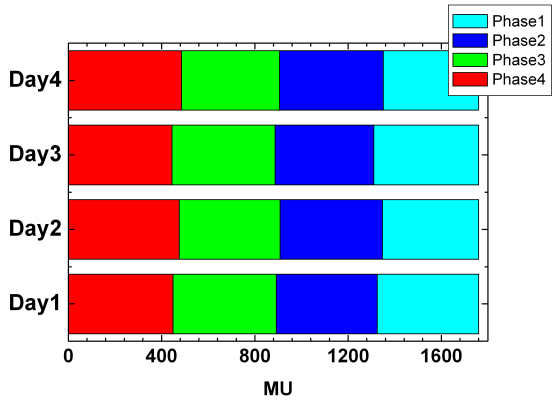

Fig. A-1: Monitor unit (MU) values divided into 4 phases for patients 1–3, who were prescribed 50 Gy for 4 fractions (2005 MU/fraction), 56 Gy for 7 fractions (1395 MU/fraction), and 50 Gy for 4 fractions (1740 MU/fraction), respectively.

Dose calculation using the above assigned MU values was performed in each phase. The results of the mean, minimum, and maximum doses in the GTV are shown in Fig. A-2, where the left panels show the absolute dose while the right panels show the dose difference inside the GTV.

Patient 1:

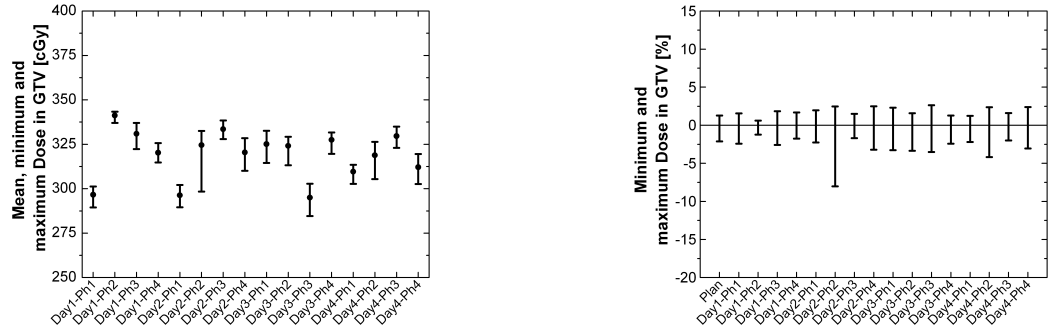

Patient 2:

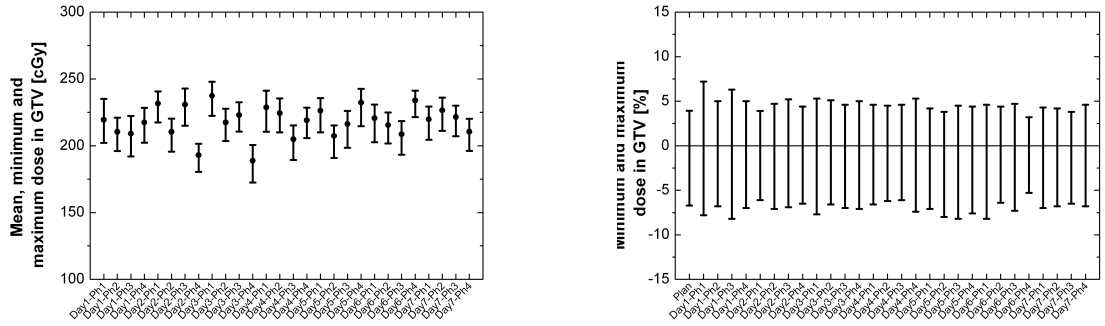

Patient 3:

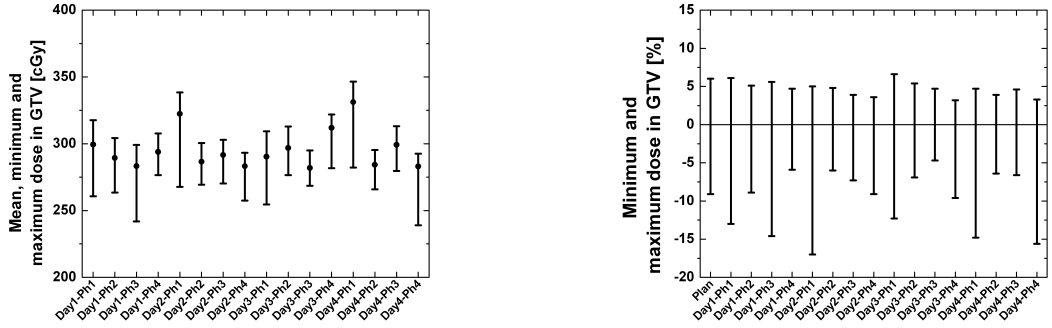

Fig. A-2: Comparison of the mean, minimum, and maximum doses in the GTV at all respiratory phases for all treatment days. In the left panel, the square boxes represent the absolute mean dose, and error bars represent the minimum and maximum dose. The right panel shows the dose difference inside the GTV.